JAMES | Journal of Advances in Modeling Earth Systems

RESEARCH ARTICLE
10.1029/2019MS001734

Key Points:
- Convection is simulated in the presence of an idealized, time-invariant, large-scale vertical velocity profile
- The resulting atmospheric state is referred to as radiative-convective-dynamical equilibrium
- This framework may be used to study convection and its interaction with the large-scale atmosphere

Correspondence to:
R. A. Warren,
rob.warren@monash.edu

Citation:
Warren, R. A., Singh, M. S., & Jakob, C. (2020). Simulations of radiative-convective-dynamical equilibrium. *Journal of Advances in Modeling Earth Systems*, *12*, e2019MS001734. https://doi.org/10.1029/2019MS001734

Received 6 MAY 2019
Accepted 29 JAN 2020
Accepted article online 31 JAN 2020

Simulations of Radiative-Convective-Dynamical Equilibrium

Robert A. Warren[1,2], **Martin S. Singh**[1,2], **and Christian Jakob**[1,2]

[1]School of Earth, Atmosphere and Environment, Monash University, Clayton, Victoria, Australia, [2]ARC Centre of Excellence for Climate Extremes, Monash University, Clayton, Victoria, Australia

Abstract Small-domain cloud-resolving model and single-column model simulations have historically applied one of three representations of large-scale vertical motion, w_{LS}. In simulations of radiative-convective equilibrium, $w_{LS} = 0$, and a balance develops between convective heating and radiative cooling. Under the weak-temperature gradient approximation and related approaches, w_{LS} is diagnosed based on the model's thermodynamic profile. Finally, for real-case simulations, w_{LS} may be prescribed as a time-varying field derived from observations. Here, we propose one additional setup, namely, a prescribed but time-invariant vertical motion. In this case, the atmosphere evolves toward an equilibrium state characterized by a three-way balance between radiative and adiabatic cooling and convective heating, with the relative contribution of radiation decreasing with increasing w_{LS}. We refer to this state as radiative-convective-dynamical equilibrium (RCDE). In this preliminary study we highlight the characteristics of the RCDE state through a suite of simulations performed with a single cloud-resolving model and single-column model. An appealing aspect of these simulations is the wide variety of equilibrium states achieved, ranging from dry and strongly unstable for small w_{LS} to approximately moist neutral for large w_{LS}. This makes RCDE a propitious framework for future model intercomparisons.

1. Introduction

Radiative-convective equilibrium (RCE) is the statistical equilibrium state achieved by a greenhouse atmosphere in the absence of lateral energy transport, wherein net radiative cooling is balanced by latent heat release (primarily associated with moist convection) and the surface sensible heat flux. It has been used as a simple idealization of the climate system in numerical modeling studies dating back to the 1960s (Manabe & Strickler, 1964; Möller, 1963). However, during the last two decades there has been a rapid increase in the number of studies employing RCE to investigate aspects of Earth's present and future climate. One area of particular focus has been the topic of convective self-aggregation in RCE, whereby initially scattered convection becomes spontaneously organized into one or more spatially coherent clusters. This behavior has been observed in a wide variety of numerical simulations (Wing et al., 2017, and references therein), although the degree to which the real atmosphere self aggregates remains a topic of active research (Holloway et al., 2017). RCE has also been used as a framework for studies looking at potential future changes in tropical convection under global warming (e.g., Cronin & Wing, 2017; Muller et al., 2011; Singh & O'Gorman, 2015).

In response to the increasing diversity of simulations applying RCE, Wing et al. (2018, hereinafter W18) initiated the radiative-convective equilibrium model intercomparison project (RCEMIP). This provides a set of standard configurations for simulating RCE across a variety of model types, including cloud-resolving models (CRMs), general circulation models (GCMs), and single-column models (SCMs). Of particular relevance to the present study are the so called `RCE_small` CRM simulations, which employ a square domain of order ~100 × 100 km^2 (roughly equivalent to a single GCM grid box) and a horizontal grid length of ~1 km. To determine the temperature dependence of the equilibrium state (including the degree of convective aggregation), all simulations are performed for three values of sea-surface temperature (SST): 295, 300, and 305 K. As well as providing a baseline for past and future studies, the results of RCEMIP will allow for a comprehensive assessment of the robustness of the RCE state, and its temperature dependence, across the spectrum of models.

While RCE is known to be a valid approximation for the global atmosphere, its applicability on smaller scales has only recently been explored. Using a combination of long-term global data sets, Jakob et al. (2019) showed that, on a daily time scale, the tropical atmosphere is near RCE around 80% of the time for spatial scales of ~5,000 × 5,000 km^2, but only around 10% of the time for spatial scales of ~100 × 100 km^2. In fact, on small scales, precipitation and radiative cooling are shown to be anticorrelated, precisely opposite to what one would expect in RCE. At larger scales, RCE is achieved through the coexistence of regions with suppressed precipitation and strong radiative cooling and regions with heavy precipitation and weak radiative cooling. The authors also show that when the atmosphere is close to RCE on small scales, it is characterized by mostly disorganized convective cloud states.

An important characteristic of RCE is that there is no net vertical mass flux. In contrast, regions of intense convective activity, such as the ITCZ, are characterized by net ascent, which acts to offset the thermodynamic imbalance between precipitation and radiation through adiabatic cooling. Similarly, regions of suppressed convection are characterized by subsidence and adiabatic warming. In SCM and CRM simulations these apparent circulations can be represented via the inclusion of an additional forcing term in the model's prognostic equations. This may take the form of an imposed "large-scale" vertical velocity profile, $w_{\mathrm{LS}}(z)$, which acts on the instantaneous local or domain-averaged fields of temperature and water vapor (and possibly other prognostics such as cloud condensate). Alternatively, one can directly prescribe the associated advective tendencies, assuming these are known. Both approaches are valid (Randall & Cripe, 1999) and have been widely used in simulations of major observational campaigns such as the Tropical Ocean Global Atmosphere Coupled Ocean-Atmosphere Response Experiment (TOGA-COARE; Webster & Lukas, 1992) (e.g., Bechtold et al., 2000; Johnson et al., 2002; Redelsperger et al., 2000), the Tropical Warm Pool International Cloud Experiment (TWP-ICE; May et al., 2008) (e.g., Davies et al., 2013; Fridlind et al., 2012; Petch et al., 2014), and the Dynamics of the Madden-Julian Oscillation (MJO) experiment (DYNAMO; Yoneyama et al., 2013) (e.g., Abdel-Lathif et al., 2018; Li et al., 2018; Wang et al., 2015).

An alternative approach to representing the connection between convection and the large-scale circulation in limited-domain models is to parameterize w_{LS} as a function of the model's thermodynamic profile. The simplest such method applies the weak-temperature gradient (WTG) approximation to diagnose w_{LS} at each time step based on the difference between the instantaneous potential temperature profile and some reference profile (Raymond & Zeng, 2005; Sobel & Bretherton, 2000). Other approaches apply an approximation of weak pressure gradients in the free troposphere (Edman & Romps, 2014; Romps, 2012a, 2012b), decompose the potential temperature anomaly into a set of vertical modes (Herman & Raymond, 2014), or relate the potential temperature anomaly to a linear gravity wave with a single wave number (Blossey et al., 2009; Kuang, 2008). All of these methods ultimately rely on the tendency for the atmosphere to rapidly remove free-tropospheric horizontal gradients of buoyancy and pressure in the deep tropics, where the Coriolis parameter is small. For intercomparisons of the different approaches the reader is directed to Daleu et al. (2015, 2016), Edman and Romps (2015), and Wang et al. (2016).

In summary, small-domain CRM and SCM simulations have historically applied one of three more or less idealized settings: no vertical motion (RCE), prescribed time-varying vertical motion (case studies), or diagnosed vertical motion (WTG and related approaches). Here we propose one additional setup, namely, a prescribed but time-invariant vertical motion. In this case, as we shall show, simulations evolve toward an equilibrium state characterized by a three-way balance between radiative and adiabatic cooling and convective heating. We refer to this state as radiative-convective-dynamical equilibrium (RCDE), although, for most of the w_{LS} magnitudes considered here, radiation represents a small component in the energy budget.

An attractive feature of RCDE is the ability to simulate a wide variety of equilibrium states, ranging from the relatively dry and weakly convecting RCE state (for $w_{\mathrm{LS}} = 0$) to a moist and intensely precipitating state more characteristic of the ITCZ (for large w_{LS}). This makes RCDE a useful framework with which to study interactions between convection and the large-scale environment. For example, in a companion study to the present work, CRM simulations of RCDE are used to investigate the relationship between precipitation and the thermodynamic structure of the atmosphere on intraseasonal and longer time scales (Singh et al., 2019). Here, we set out the simulation framework and illustrate its utility through comparison of results from a single CRM and SCM. We begin in section 2 by describing the simulation setup, in particular the implementation of large-scale vertical advection. Section 3 then provides details of the CRM and SCM used

in our preliminary simulations, with results presented in section 4. Finally, in section 5, conclusions are drawn, and avenues for further work are highlighted.

2. Simulation Design

The design of our simulations is identical to the `RCE_small` configuration described in W18 but with the addition of a large-scale vertical velocity. Initial profiles of temperature T and specific humidity q are specified using analytical functions designed to approximate the moist tropical sounding of Dunion (2011). The initial pressure profile is then retrieved using hydrostatic balance, while zonal and meridional winds are set to zero. To expedite convective initiation in the CRM simulations, random thermal noise, with a maximum amplitude of 0.1 K, is added in the lowest five model levels. The surface boundary condition is a spatially uniform fixed SST. Rotation is neglected by setting the Coriolis parameter to zero. Shortwave and longwave radiative heating rates are calculated interactively with fixed trace gas concentrations and an analytical ozone profile. Incoming solar radiation is specified as spatially uniform and constant in time, using a reduced solar constant of 551.58 W/m^2 and a fixed zenith angle of 42.05°. These values give a top-of-atmosphere insolation of 409.6 W/m^2, equivalent to the tropical (0–20°) annual mean. The surface albedo is set to the insolation-weighted global average value of 0.07.

The large-scale vertical velocity w_{LS} is specified as a half sine wave with amplitude w_{max}, extending from the surface to $z = H$:

$$w_{\mathrm{LS}}(z) = \begin{cases} w_{\mathrm{max}} \sin\left\{\frac{\pi z}{H}\right. & \text{for } 0 \le z \le H, \\ 0 & \text{for } z > H. \end{cases} \tag{1}$$

The associated large-scale vertical advection is represented by adding the following terms to the model's prognostic equations for potential temperature θ and mixing ratio r:

$$\left(\frac{\partial \theta}{\partial t}\right)_{\mathrm{LS}} = -w_{\mathrm{LS}} \frac{\partial \bar{\theta}}{\partial z}, \tag{2}$$

$$\left(\frac{\partial r}{\partial t}\right)_{\mathrm{LS}} = -w_{\mathrm{LS}} \frac{\partial \bar{r}}{\partial z}. \tag{3}$$

Here, overlines indicate a horizontal average over the CRM domain (for the SCM, $\bar{\theta} = \theta$ and $\bar{r} = r$). Horizontal variations in θ and r in the CRM are therefore neglected, with the same advective tendency applied at all grid points on a given model level. Vertical advection of momentum and liquid and ice condensate are also neglected.

A further simplification in (2) and (3) is that differences in temperature and moisture between the simulated column and the surrounding atmosphere are small. This assumption is implicitly made for θ in WTG simulations; however, different approaches have been taken to represent the horizontal advection of r. These include "lateral entrainment," where air with mixing ratio r_{ref} is drawn into the domain at levels of large-scale vertical mass divergence (e.g., Herman & Raymond, 2014; Raymond & Zeng, 2005; Sessions et al., 2010), and "relaxation," where r is relaxed to r_{ref} over a specified time scale (e.g., Sobel et al., 2007; Sobel & Bellon, 2009; Wang & Sobel, 2012). In both cases, the reference mixing ratio profile is typically taken from a corresponding RCE simulation. Other studies have taken the simple approach used here and neglected horizontal moisture advection (e.g., Anber et al., 2014; Wang & Sobel, 2011; Wang et al., 2013). A comparison of the three approaches for a suite of 2-D CRM simulations is presented in Sessions et al. (2015).

As in RCEMIP, three different values of SST are considered (295, 300, and 305 K), with corresponding initial values of surface q (12, 18.65, and 24 g/kg) chosen such that the near-surface relative humidity (RH) is close to 80%. Here we also consider a range of large-scale forcing (LSF) magnitudes by varying w_{max} from zero (the RCE case) to 5 cm/s in increments of 1 cm/s. Note that we also vary H with the SST to be roughly consistent with the tropopause height in RCE (H = 11, 12.5, and 14 km for the 295, 300, and 305 K runs, respectively). The combination of three different SSTs and six different forcing magnitudes gives us a total of 18 simulations. Each of these is given a unique identifier of the form Ta-Wb where a is the SST in K and b is w_{max} in cm/s.

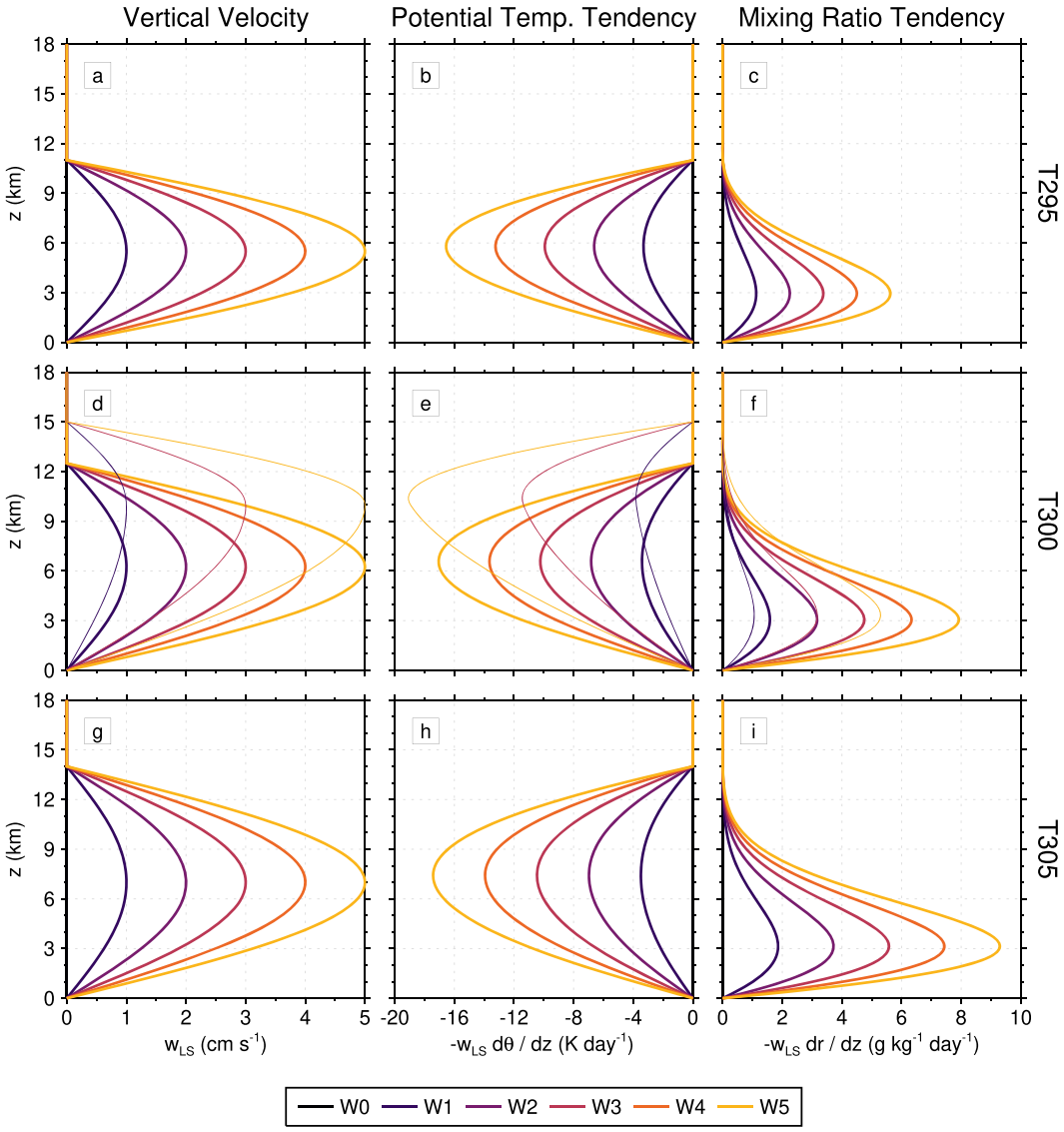

Figure 1. Vertical profiles of (left) large-scale vertical velocity and associated initial tendencies of (middle) potential temperature and (right) water vapor mixing ratio for simulations with SSTs of (top to bottom) 295, 300, and 305 K. Thin lines in d–f show profiles for the top-heavy LSF simulations.

Figure 1 shows the w_{LS} profiles and associated initial advective tendencies for each of these simulations. Vertical advection is associated with cooling and moistening, which increases linearly with w_{LS}; however, the vertical structure of the tendencies and their dependence on SST differ. Since the initially imposed temperature lapse rate is almost constant, the large-scale θ tendency essentially mirrors the w_{LS} profile, with the strongest cooling located just above $H/2$. It also shows limited dependence on SST. On the other hand, $\partial r/\partial z$ varies strongly with height such that the large-scale moisture tendency peaks at around 3 km for all three SSTs, while its magnitude increases strongly with SST. It is emphasized that the tendencies shown in Figure 1 only apply on the first model time step; after this, they will evolve in response to changes in the profiles of $\bar{\theta}$ and $\bar{r}$ as the simulations progress.

We note that the shape of our w_{LS} profiles, with peak values in the midtroposphere, corresponds to the first baroclinic mode. In contrast, large-scale vertical velocity profiles observed in the deep tropics during periods of active convection tend to be more top heavy, with a peak around 10 km (~300 hPa), reflecting a combination of the first and second baroclinic modes. To explore the impact of this difference, additional

simulations were performed using a modified w_{LS} profile specified as

$$w_{LS}(z) = \begin{cases} w_{max} & \sin\left[\frac{\pi}{2}\left[\frac{z}{z_{max}}\right]\right] & \text{for } 0 \le z < z_{max} \\ w_{max} & \cos\left[\frac{\pi}{2}\left[\frac{z-z_{max}}{z_{top}-z_{max}}\right]\right] & \text{for } z_{max} \le z \le z_{top} \\ 0 & & \text{for } z > z_{top}, \end{cases} \quad (4)$$

where $z_{max} = 10$ km and $z_{top} = 15$ km. These values were chosen to provide a reasonable match to observed w_{LS} profiles associated with heavy precipitation (≥10 mm/day) during the TOGA-COARE, TWP-ICE, and DYNAMO field campaigns (not shown). Simulations were performed with an SST of 300 K for w_{max} values of 1, 3, and 5 cm/s.

The profiles of w_{LS} and corresponding initial θ and r tendencies for these top-heavy LSF simulations are shown by the thin lines in Figure 1. We see that, for a given w_{max}, the peak potential temperature forcing shifts upward and increases in magnitude, resulting in smaller tendencies in the lower troposphere and much larger tendencies in the upper troposphere. Conversely, the water vapor forcing maintains a similar peak but with reduced amplitude. Overall, the results of these runs were broadly consistent with the standard LSF simulations and thus will not be discussed at length herein. The only noteworthy difference was a significant increase in anvil-level cloud in the CRM simulations (see section 4.3). This promotes longwave radiative heating in the upper troposphere; however, the net effect on the column integrated energy budget is small compared to the direct effect of changing the forcing.

3. Models

CRM simulations are performed with Cloud Model 1 (CM1), Release 19 (Bryan & Fritsch, 2002; Bryan, 2017). The model is configured to solve the compressible governing equations on a three-dimensional domain of $96 \times 96 \times 28$ km^3, with periodic lateral boundaries, a rigid semislip lower boundary (Coffer & Parker, 2017), and a rigid free-slip upper boundary. Fixed horizontal grid spacing of 1 km is used together with a stretched vertical grid with 68 levels. Vertical grid spacing increases from 20 m at the surface to 500 m at 5.5 km and is constant thereafter. Rayleigh damping (with a time scale of 300 s) is applied above 24 km to prevent spurious reflection of wave energy. Temporal integration is performed using a Klemp-Wilhelmson time-splitting scheme (Klemp & Wilhelmson, 1978) with a vertically implicit solver and adaptive time stepping. Implicitly diffusive fifth-order advection is used in both the horizontal and vertical with no additional explicit diffusion. For all scalars except pressure, a weighted essentially nonoscillatory scheme (Borges et al., 2008; Jiang & Shu, 1996) is applied on the final acoustic time step. Subgrid mixing is parameterized using a turbulent kinetic energy scheme (Deardorff, 1980), and surface exchange is represented using the revised Weather Research and Forecasting (WRF) model scheme of Jiménez et al. (2012). Radiation is parameterized using the Rapid Radiative Transfer Model for GCMs scheme adapted from WRF, with tendencies updated every 300 s. Microphysical processes are represented using the Morrison double-moment scheme (Morrison et al., 2005), which includes five prognostic water species: cloud water, cloud ice, rain, snow, and graupel.

SCM simulations are performed using the Global Atmosphere 7.1 configuration of the Met Office Unified Model (UM; Walters et al., 2019). The domain is a single column with 85 vertical levels extending from the surface to an altitude of 80 km. The model time step is 1,200 s. Radiative transfer is parameterized using the SOCRATES scheme (Edwards & Slingo, 1996; Manners et al., 2015) with calculations performed every hour using the instantaneous cloud field. Large-scale cloudiness is represented using the prognostic cloud fraction and prognostic condensate scheme (Wilson et al., 2008b, 2008a), together with the cloud erosion parameterization described by Morcrette (2012) and critical RH parameterization of Van Weverberg et al. (2016). The microphysics parameterization is based on Wilson and Ballard (1999) and includes three prognostic water species: cloud water, ice, and rain. Local and nonlocal turbulent mixing is represented using the first-order scheme of Lock et al. (2000) with modifications described by Lock (2001) and Brown et al. (2008). Convection is parameterized using a mass-flux scheme based on Gregory and Rowntree (1990) with a convective available potential energy (CAPE) closure for cloud-base mass flux (Fritsch & Chappell, 1980).

For both models, the full suite of simulations is run out to 100 days with hourly output. We note that for RCEMIP, W18 recommend running SCM simulations out to 1,000 days; however, we found that 100 was

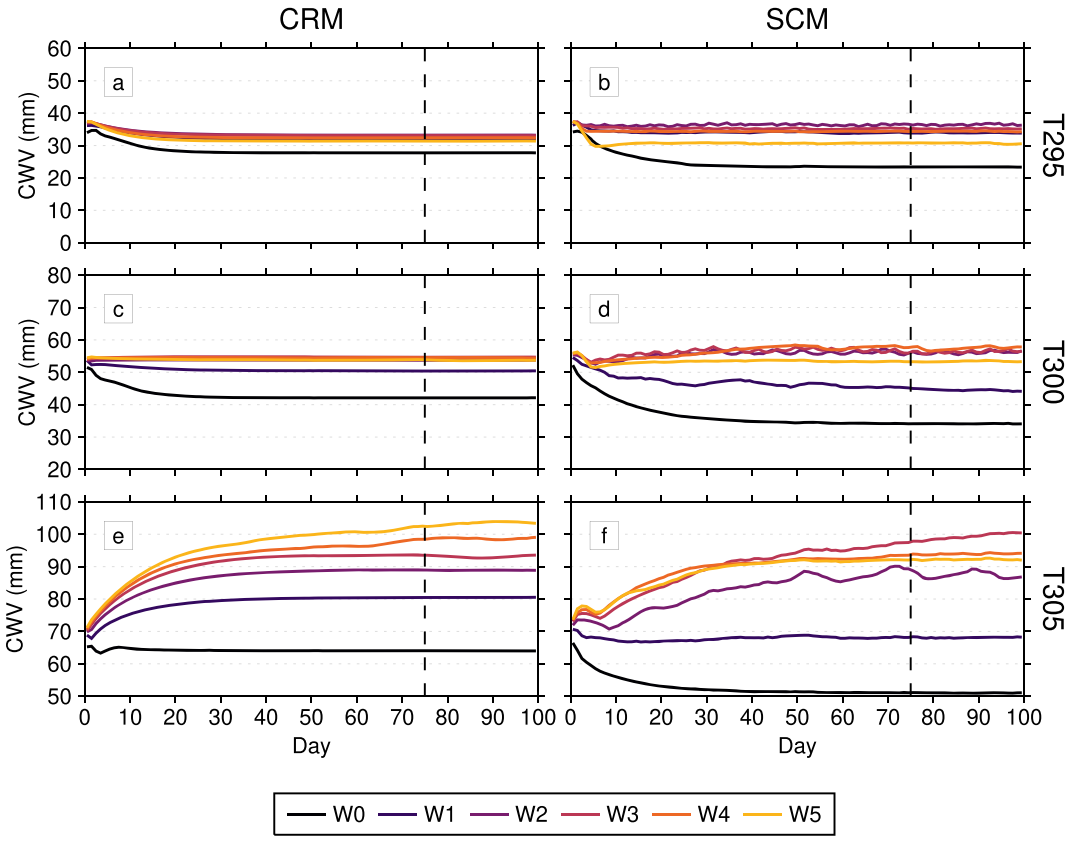

Figure 2. Time series of daily-mean column water vapor (CWV) from (left) CRM and (right) SCM simulations with SSTs of (top to bottom) 295, 300, and 305 K.

sufficient to reach equilibrium in most cases. Modifications were made to CM1 to allow for the output of temporally and horizontally averaged diagnostics as requested for RCEMIP (Wing et al., 2018, their Tables 4–7). On the other hand, for the UM, the standard SCM output fields were simply postprocessed to derive the required diagnostics. One key difference compared to W18 is that, for our CRM runs, we output 2-D (x-y) variables as instantaneous fields rather than hourly averages. This allows us to examine the structure of the convective precipitation and associated circulations at specific instances during the simulations.

4. Results

4.1. Approach to Equilibrium

We begin by examining the development of the equilibrium state in our simulations. This is illustrated in Figure 2, which shows time series of daily-mean column water vapor (CWV) for the 18 CRM and SCM runs. Within the first 50 days, nearly all of the CRM simulations reach a state characterized by essentially constant CWV. However, in the high-SST case (T305), the most strongly forced runs (W3–5) show pronounced fluctuations in CWV, which persist until the end of the simulations. These are associated with the development of organized convective structures. Figure 3 shows 2-D snapshots of 10 m winds and surface rain rate at $t = 100$ days from a subset of the CRM simulations. At all three SSTs, the RCE simulations are characterized by small and widely scattered showers with roughly circular divergent outflows. With increasing LSF, convection in the T295 and T300 runs becomes more widespread but remains largely disorganized. However, in the T305 runs we find the emergence of organized clusters of convection, with broader areas mostly devoid of precipitation. As shown in Figure 4, low-level winds are significantly stronger and more variable in these runs, reflecting the presence of coherent mesoscale convective outflows. These winds drive fluctuations in the surface latent heat flux (not shown), which seem to account for the unsteady evolution of CWV. Further investigation of the organization of convection in these runs is presented in section 4.6.

Returning to Figure 2, we note that many (though not all) of the SCM runs feature quasi-periodic fluctuations in CWV on time scales of around 3–20 days. These appear to be linked to similar periodicity in the

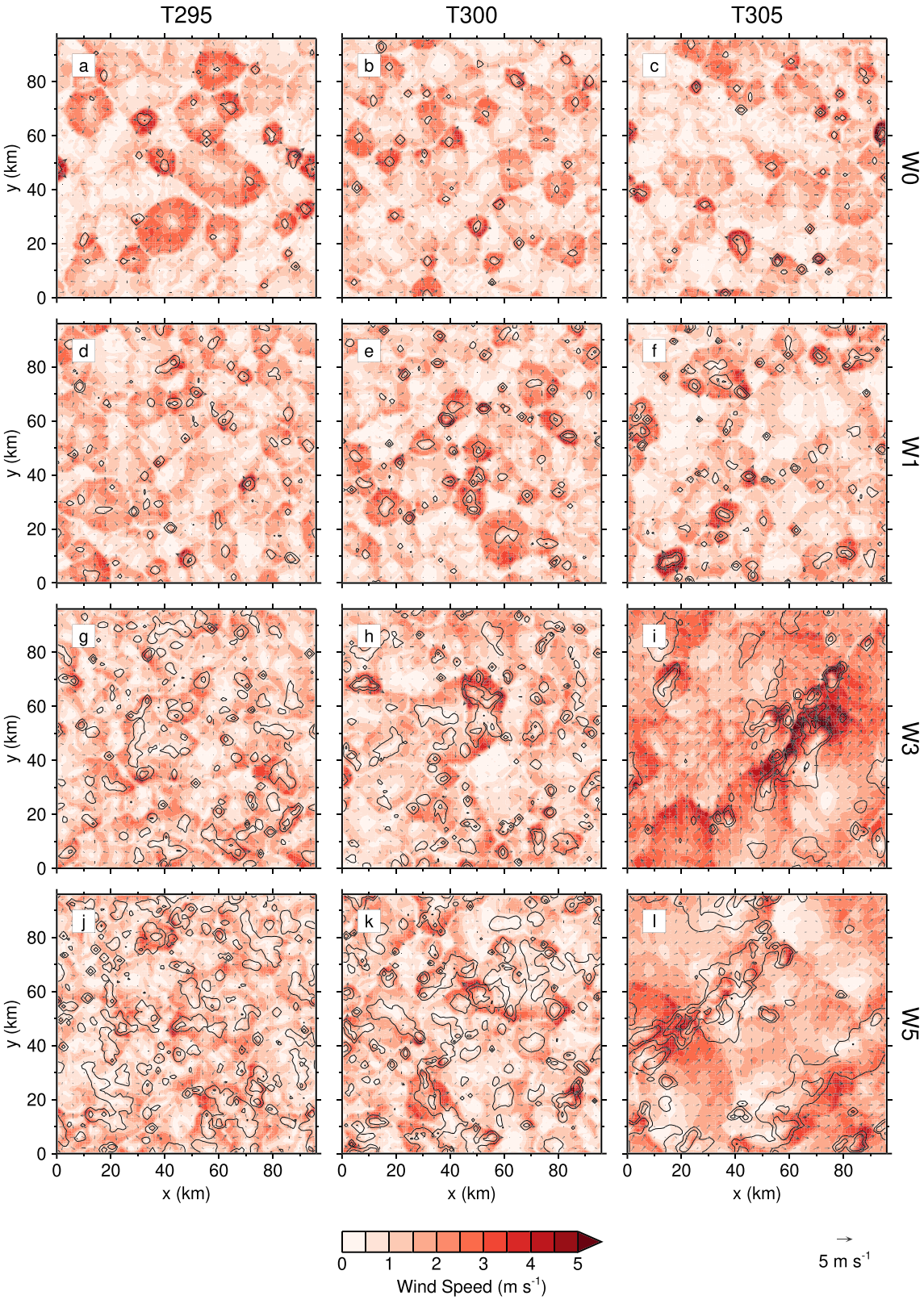

Figure 3. Maps of instantaneous 10 m winds (colors and vectors) and surface precipitation rate (contours at 1 and 10 mm/hr) at t = 100 days for the CRM simulations with SSTs of (left to right) 295, 300, and 305 K, and LSF magnitudes of (top to bottom) 0, 1, 3, and 5 cm/s.

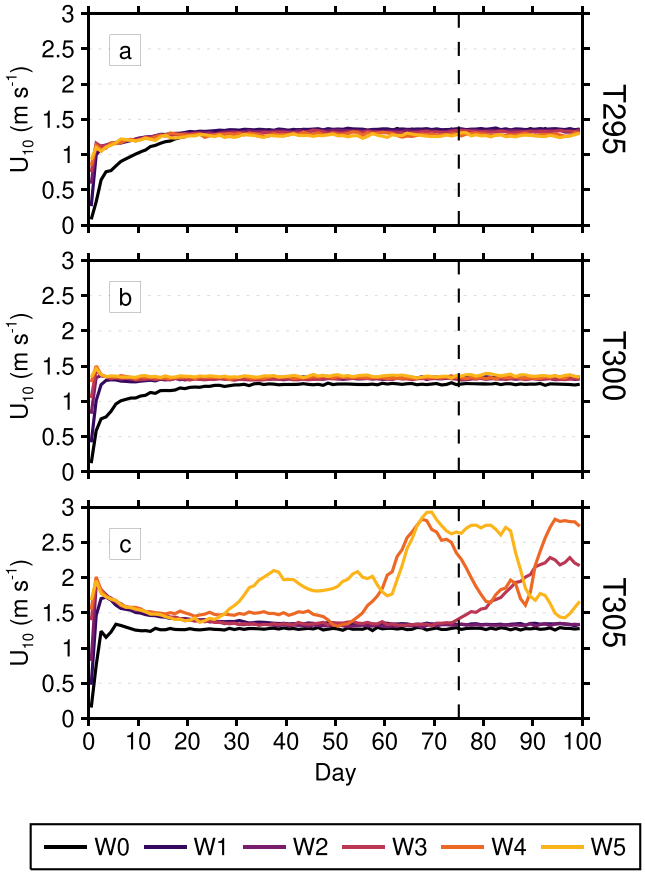

Figure 4. Time series of daily-mean 10 m wind speed from the CRM simulations with SSTs of (top to bottom) 295, 300, and 305 K.

frequency with which the model's convection scheme operates (Figure 5). This behavior is most pronounced in the simulations with intermediate LSF (W2 and W3), with the weakly and strongly forced runs displaying much smaller variations. Intermittency is a known issue with the UM convection scheme (e.g., Martin et al., 2017) resulting from the choice of closure. When called, the scheme tends to modify the thermodynamic profile such that convection cannot trigger on the next time step. The overall frequency with which the scheme operates depends on the balance between generation of instability through heating of the boundary layer and cooling of the free troposphere (by radiation and/or large-scale ascent) and the removal of instability by convection. In our weak-LSF runs it appears that the stabilizing effect of convection dominates, leading to a consistently low triggering frequency of ~20%. On the other hand, rapid destabilization in the strong-LSF runs promotes a consistently high triggering frequency around 60%. The intermediate-LSF cases seem to represent a transition between these two regimes, characterized by large, quasi-periodic variations in triggering frequency.

In the remainder of our analysis, we consider time-averaged quantities, computed over the final 25 days of each simulation, which is taken to represent the equilibrium state. However, it is clear from Figure 2 that in some of the high-SST runs, the atmosphere has not reached a stable equilibrium by this point. In particular, the T305–W3, T305–W4, and T305–W5 CRM simulations and the T305–W3 and T305–W4 SCM simulations are characterized by fluctuations, which appear to be either aperiodic or very low frequency. To explore this issue further, these simulations were extended: out to 200 days for the CRM runs and 1,000 days for the SCM runs. The extended CRM runs suggest that the fluctuations in CWV are indeed aperiodic and reveal a slight increasing trend in CWV during the t = 100–200 day period (not shown). For the extended SCM runs we find continued increases in CWV up to around t = 600 days, after which values seem to equilibrate at around 110 and 107 mm for the W3 and W4 runs, respectively (not shown). Some care must therefore be taken in interpreting the results for these runs.

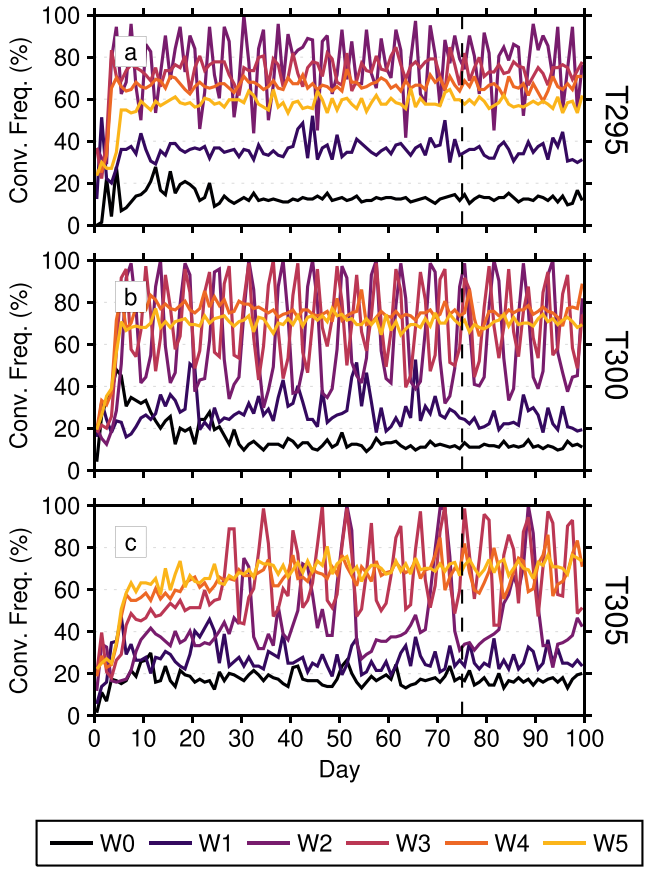

Figure 5. Time series of the frequency with which the SCM convection scheme is triggered (expressed as the percentage of time steps per day) for simulations with SSTs of (top to bottom) 295, 300, and 305 K.

4.2. Equilibrium Thermodynamic Profiles

In this section we examine the vertical structure of the atmosphere at equilibrium, starting with the RCE runs. Figure 6 shows vertical profiles of temperature, mixing ratio, and moist static energy (MSE) for each of the CRM and SCM RCE runs, together with the corresponding initial profiles. MSE (in J/kg) is given by $h = c_p T + gz + L_v r$, where c_p is the heat capacity of dry air at constant pressure, g is the acceleration due to gravity, and L_v is the latent heat of vaporization. In Figure 6, h is normalized by c_p, giving units of Kelvin. We see that the RCE state is characterized by pronounced cooling relative to the initial profile. This is generally accompanied by a decrease in mixing ratio, consistent with the trends in CWV seen in Figure 2, although in the T305 CRM simulation r increases above ~3 km. Together, these changes result in a strong reduction in MSE relative to the initial state, except in the midtroposphere in the T305 CRM run. Comparing the CRM and SCM simulations, we note that the latter are both cooler and drier and are characterized by more pronounced vertical structure, in particular, a local minimum in the lapse rates of T and r at the freezing level.

Figures 7 and 8 illustrate how these profiles change in response to LSF. Focusing first on the CRM simulations (Figure 7), we observe warming in most of the free troposphere and cooling near the surface and in the stratosphere. The degree of warming in the troposphere increases with height, indicating a stabilization of the column. The mixing ratio increases at all levels, except near the boundary-layer top in the strongly forced T295 simulations. MSE increases fairly uniformly across the free troposphere, with smaller changes in the boundary layer. There is a strong increase in the magnitude of the changes with SST, with maximum values for T and r increasing from around 3 K and 1 g/kg in the T295 runs to around 20 K and 7 g/kg in the T305 runs. The dependence on LSF also varies with SST: In the T295 and T300 runs the largest changes are associated with intermediate forcing, whereas in the T305 runs there is a monotonic increase with LSF. Results for the SCM simulations (Figure 8) are qualitatively similar, but the magnitude of the changes is generally larger. We also note that, in contrast to the CRM simulations, the trends with LSF for the T305

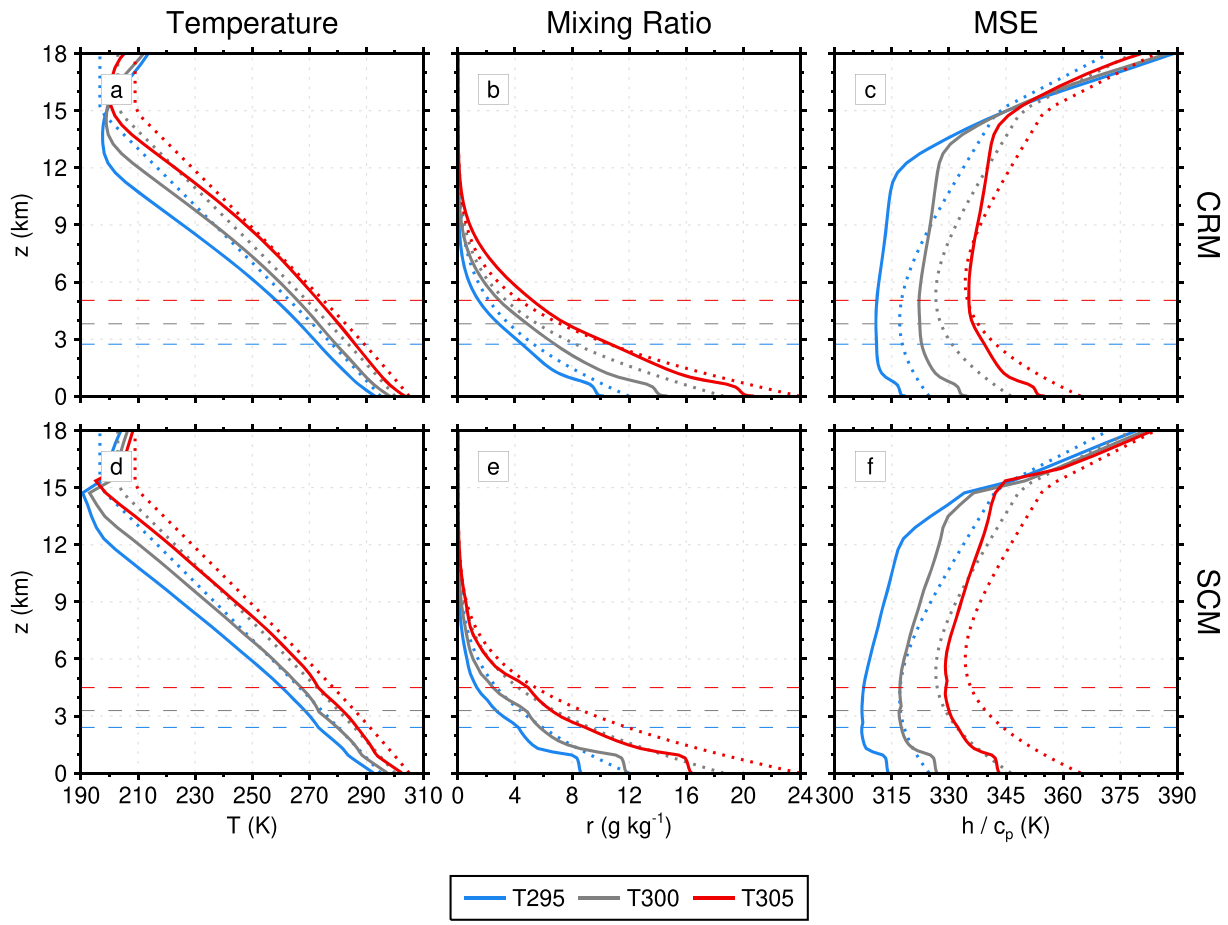

Figure 6. Vertical profiles of (left) temperature, (middle) mixing ratio, and (right) MSE for (top) CRM and (bottom) SCM RCE simulations. Dotted lines show the prescribed initial profiles, and solid lines show the equilibrium profiles averaged over the final 25 days of each simulation. Dashed horizontal lines show the equilibrium freezing-level height.

runs are nonmonotonic (cf. Figure 2). This nonmonotonicity likely reflects complex feedbacks between the LSF tendencies and the temperature and moisture profiles (via equations (2) and 3) during the approach to equilibrium.

Figure 9 compares the RH profiles across all 18 simulations. In the CRM runs, there is a clear, monotonic increase in RH with LSF over much of the column. The change is particularly pronounced between the W0 and W1 simulations, indicating that even a small amount of forcing substantially increases RH compared to the RCE state. In the strongly forced runs, the atmosphere actually becomes supersaturated (with respect to ice) in the middle troposphere, with the degree of supersaturation increasing with decreasing SST. A supersaturated layer also exists near the tropopause in all runs, presumably reflecting the presence of long-lived cirrus anvils at cloud top. We note that in the T305 runs, there is a pronounced upward shift in this anvil layer with increasing LSF, with the biggest change again occurring between the W0 and W1 simulations. A similar but smaller increase is seen in the T300 runs, while in the T295 runs the trend is actually reversed, although it is also very small. Turning to the SCM profiles, we see significant differences in the vertical structure of RH, particularly in the RCE simulations. These include lower values at the surface and in the middle troposphere, higher values at the boundary-layer top, and a deeper saturated layer in the upper troposphere. Nevertheless, the above-noted trends in RH with LSF are largely consistent between the two models, at least above the freezing level; at lower altitudes, the SCM displays nonmonotonic changes with increasing LSF.

Singh et al. (2019) present a simple steady state bulk-plume model for the thermodynamic structure of a convecting atmosphere under the influence of large-scale vertical motion. Approximating RH as $\mathcal{R} = q/q^*$,

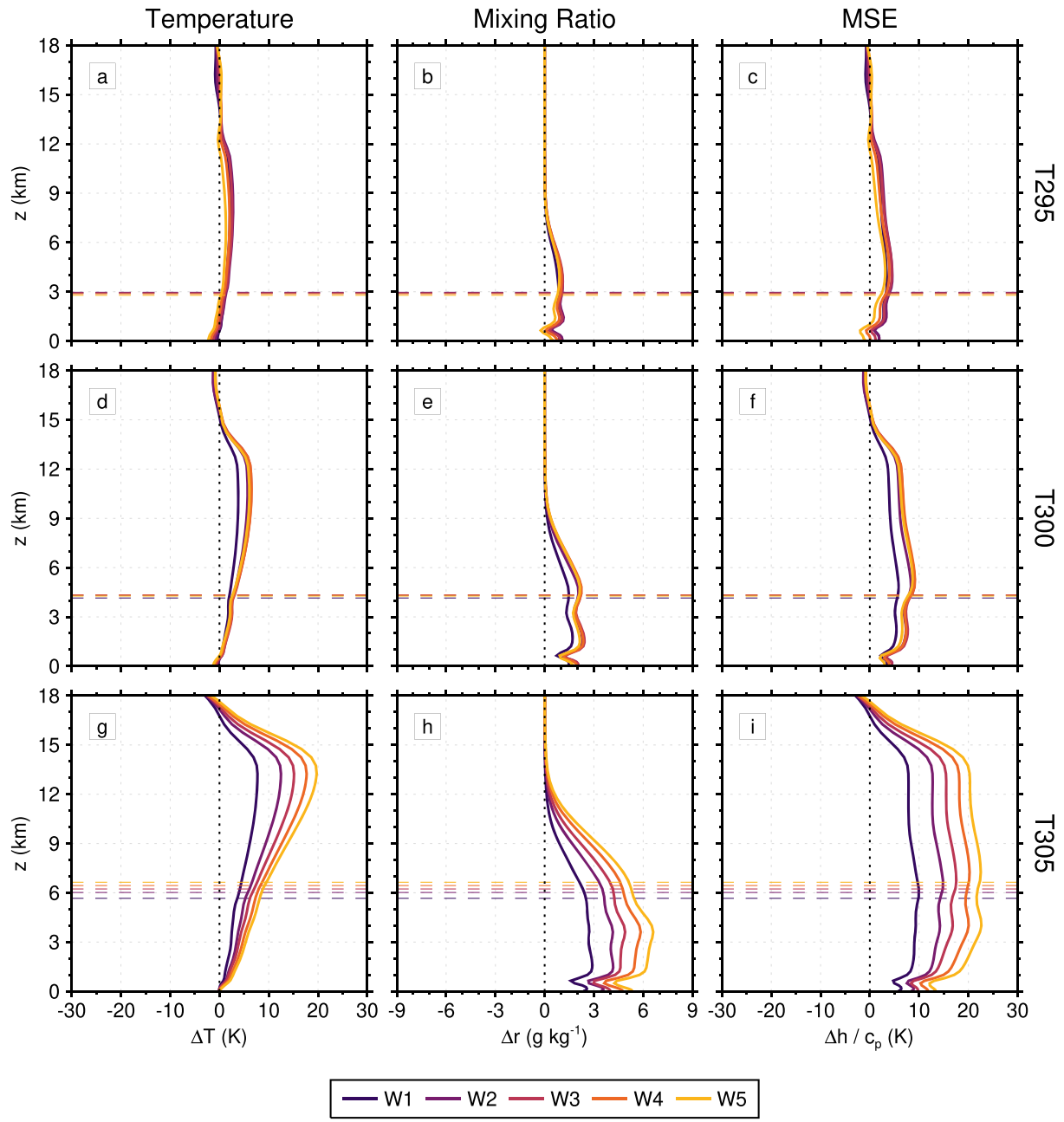

Figure 7. Vertical profiles of the difference (with respect to the corresponding RCE simulations) in (left) temperature, (middle) mixing ratio, and (right) MSE for the LSF CRM simulations at SSTs of (top to bottom) 295, 300, and 305 K. Dashed lines show the freezing-level height. All quantities are averaged over the final 25 days of each simulation.

where q^* is the saturation specific humidity, they obtain the following diagnostic equation:

$$\mathcal{R} = \frac{\delta}{\delta + m\gamma}. \tag{5}$$

Here, δ is the fractional detrainment rate, $\gamma = -\partial\left(\ln q^*\right)/\partial z$ is the fractional vertical gradient of saturation specific humidity, and $m = M_d/M_u$ is the ratio of the downward mass flux in the environment to the upward mass flux within cloud. This expression is a generalization of the one derived by Romps (2014) for an atmosphere in RCE ($m = 1$). We see that $\mathcal{R}$ is determined by the balance between moistening through convective detrainment and drying through subsidence. With increasing LSF, m decreases (implying a weakening of the subsidence drying relative to the detrainment moistening), and RH increases. Using the zero-buoyancy

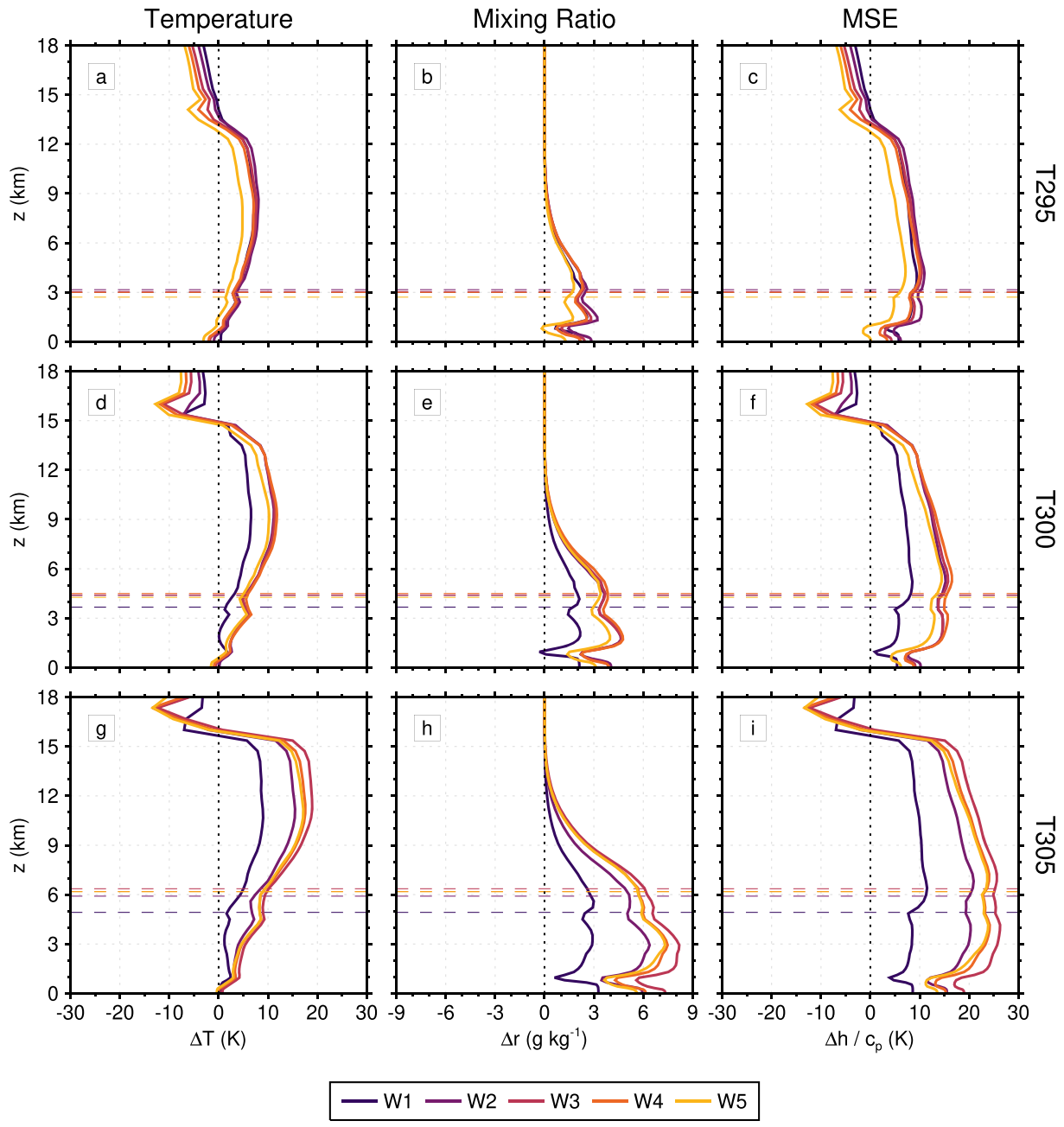

Figure 8. As in Figure 7 but for the LSF SCM simulations.

plume model of Singh and O'Gorman (2013) to parameterize γ and assuming $\delta \approx \epsilon$, the fractional entrainment rate (which is assumed constant), Singh et al. (2019) obtain analytical RH profiles, which capture the basic structure and variations with LSF shown in Figure 9 (cf. their Figure 5b).

4.3. Energy Budget

In this section we consider the budget of dry static energy, $s = c_p T + gz$, and its variation with LSF amplitude. Defining the mass-weighted column integral of a quantity χ as

$$\langle \chi \rangle = \int_0^{z_t} \rho \chi dz, \tag{6}$$

where z_t is the model top, we have

$$\left\langle \frac{\partial \bar{s}}{\partial t} \right\rangle = -\left\langle w_{LS} \frac{\partial \bar{s}}{\partial z} \right\rangle + \langle Q_R \rangle + H + L_v P. \tag{7}$$

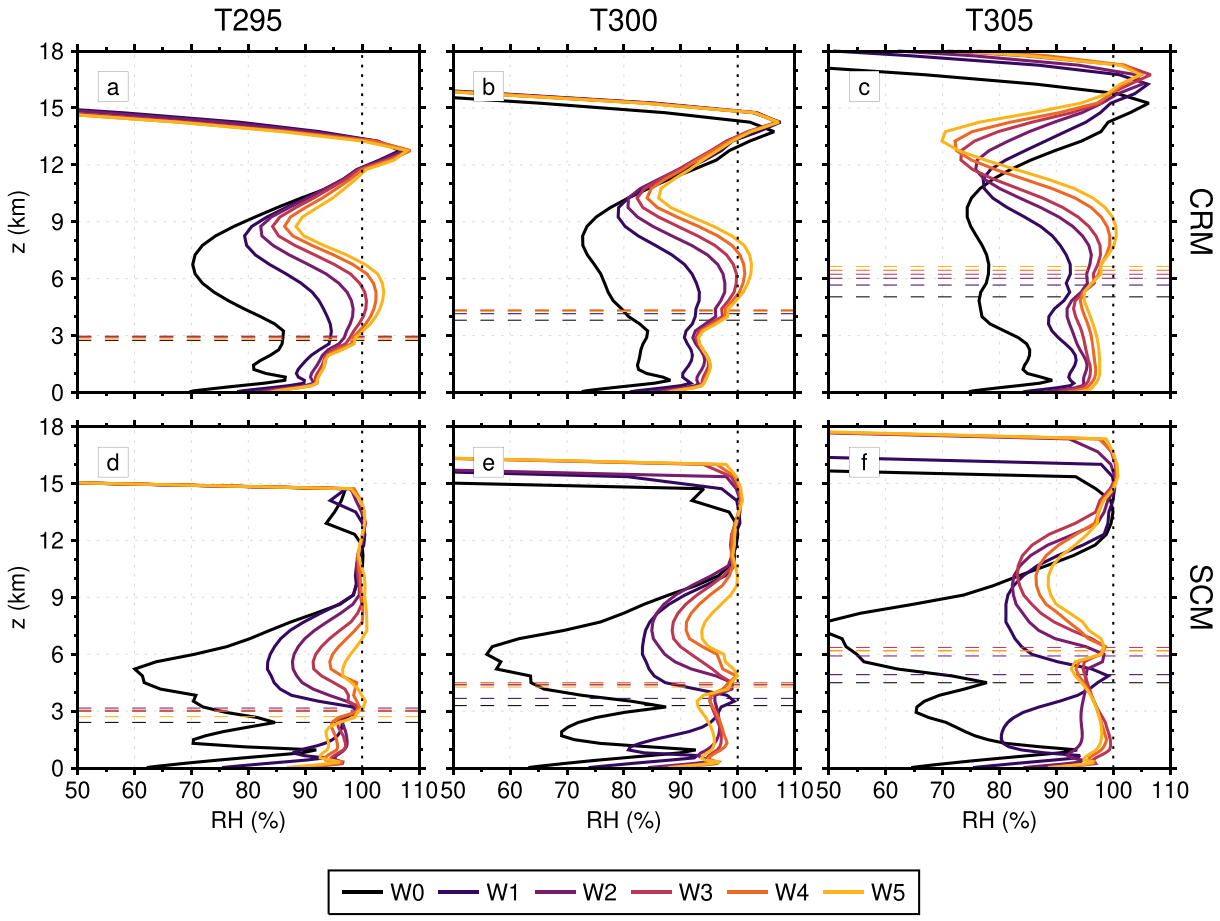

Figure 9. Vertical profiles of relative humidity (RH; computed with respect to water for $T \geq 0$ ° C and with respect to ice for $T < 0$ ° C) for (top) CRM and (bottom) SCM simulations at SSTs of (left to right) 295, 300, and 305 K. Dashed lines show the freezing-level height. All quantities are averaged over the final 25 days of each simulation.

Here Q_R is the radiative heating rate, H is the surface sensible heat flux, and P is the surface precipitation rate. The first and last terms on the right-hand side represents, respectively, the adiabatic cooling associated with LSF and convective heating through condensation. At equilibrium, the left-hand side vanishes, and we are left with a balance between forcing, radiation, surface heat flux, and precipitation. These terms are computed for each of the CRM and SCM simulations and are plotted as a function of w_{LS} in Figure 10. The heat flux represents a very small term in the budget (~5–25 W/m^2) and is therefore excluded from this analysis.

By definition, the LSF tendency is zero in the RCE simulations, giving rise to a balance between radiative cooling and precipitation. However, with the introduction of large-scale ascent the dominant balance rapidly transitions to one between precipitation and forcing. As we would expect, the magnitude of the LSF term increases with both w_{max} and SST (cf. Figure 1), with a corresponding increase in precipitation, while the radiative tendency remains small. For the CRM simulations, the contribution of radiation to the total cooling decreases from around a third in the W1 runs to less than 10% in the W5 runs. The radiative cooling term is smaller in the SCM simulations and shows a more pronounced positive trend with increasing LSF such that it actually becomes positive (indicating net radiative heating) in T295–W4 and T295–W5 runs. This trend is associated with longwave heating around the freezing level in the SCM simulations, which increases in magnitude with increasing LSF and decreasing SST (not shown).

The differences in radiative cooling between the CRM and SCM simulations can be understood by comparing profiles of cloud fraction. Following W18, the presence of cloud in the CRM is defined where the total cloud water mixing ratio exceeds 0.01 g/kg or 1% of the saturation mixing ratio over water, whichever is

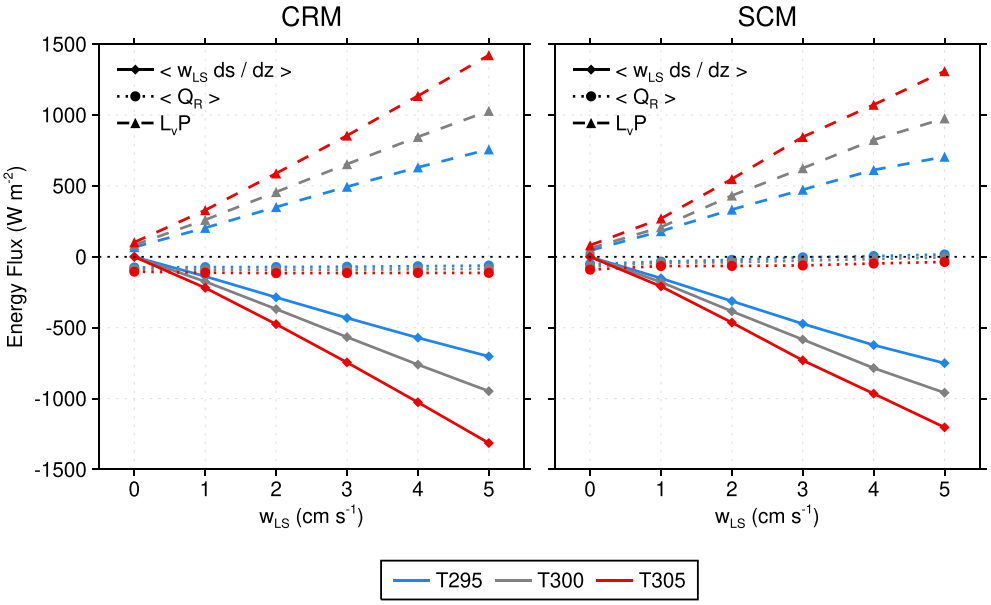

Figure 10. Contribution of large-scale forcing (solid lines with diamonds), radiation (dotted lines with circles), and precipitation (dashed lines with triangles) to the column-integrated dry static energy budget for (left) CRM and (right) SCM simulations as a function of w_{LS}. All quantities are averaged over the final 25 days of each simulation.

smaller. As shown in Figure 11, the SCM simulations are characterized by significantly larger cloud fractions, especially around the freezing level and in the upper troposphere. The SCM clouds also extend to a higher altitude. As a result, both downwelling shortwave radiation and outgoing longwave radiation (OLR) are reduced in the SCM relative to the CRM. It is interesting to note that, in the CRM, cloud fraction in the upper troposphere remains below 100% even in the presence of strong forcing. This seems to reflect our choice of w_{LS} profile. In the T300 simulations with top-heavy forcing, 100% cloud cover is observed around 13–14 km, even for weak LSF (thin lines in Figures 11b and 11e). However, as noted in section 2, this does not significantly impact the energy budget (not shown).

4.4. Variations With SST and LSF

In this section we focus on a selection of key diagnostics and explore the trends associated with increasing SST and LSF. Figure 12 plots four quantities—precipitation rate P, CAPE, column relative humidity (CRH), and CWV—as a function of SST for each of the different forcing magnitudes. Starting with P (Figure 12a), we see the expected increase with both SST and LSF. A significant feature is the increase in the slope of the lines with forcing magnitude. For the CRM, the scaling of P with SST increases from 4.9%/K (i.e., less than Clausius-Clapeyron) in the RCE case to 8.8%/K (i.e., greater than Clausius-Clapeyron) under the strongest forcing. This highlights the importance of the dynamical contribution to future changes in local precipitation (O'Gorman & Schneider, 2009). The SCM results closely match those from the CRM, which is to be expected for precipitation since it is primarily driven by the imposed forcing. The slightly lower values of P in the SCM runs can be explained by lower radiative cooling rates compared to the CRM runs (Figure 10) and differences in the equilibrium mixing ratio profile (Figures 6–8), which determines the import of moisture by the imposed circulation via equation (3).

For CAPE (Figure 12b), we observe a positive trend with SST, consistent with previous CRM studies under RCE (e.g., Muller et al., 2011; Romps, 2011), but a negative trend with LSF, indicating that the atmosphere becomes more stable under large-scale ascent. The decrease in CAPE with LSF is more dramatic in the SCM, consistent with the high frequency of convective triggering in the strongly forced runs (Figure 5): Significant instability is unable to develop as it is rapidly consumed by the convection scheme. As discussed in Singh et al. (2019), the variation of CAPE with SST and LSF may be understood by considering how convective entrainment affects the lapse rate in RCDE using the zero-buoyancy plume model of Singh and O'Gorman (2013). Specifically, if it is assumed that convective processes maintain a thermal structure that is approximately neutral with respect to an entraining plume, an equation for the saturation MSE h^* of the

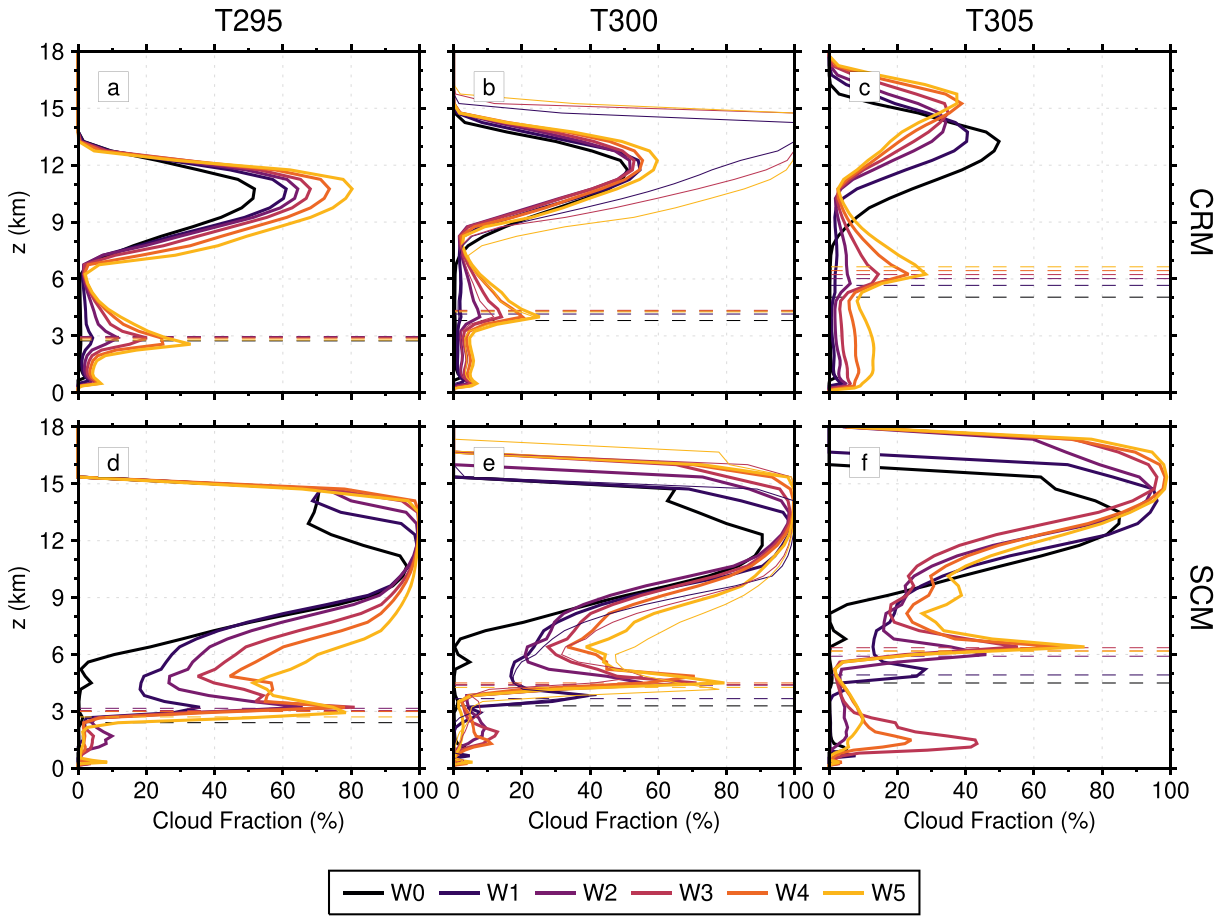

Figure 11. Vertical profiles of cloud fraction for (top) CRM and (bottom) SCM simulations at SSTs of (left to right) 295, 300, and 305 K. Thin lines in (b) and (e) show profiles for the top-heavy LSF simulations. Dashed lines show the freezing-level height (not included for the top-heavy LSF simulations). All quantities are averaged over the final 25 days of each simulation.

RCDE state may be derived:

$$\frac{\partial h^*}{\partial z} = -\epsilon L_v q^* (1 - \mathcal{R}) . \tag{8}$$

According to this equation, entrainment leads to a decrease in h^* with height, with the magnitude of this decrease depending on the saturation deficit of the environment. Since a state of moist neutrality (i.e., zero CAPE) corresponds roughly to a vertically constant h^*, this implies that the deviation from moist neutrality increases with temperature following Clausius-Clapeyron scaling (Seeley & Romps, 2015; Romps, 2016) and decreases with LSF via equation (5).

Turning to the moisture variables (Figures 12c and 12d), in the CRM simulations, CRH shows a slight increase with SST across the full range of LSF magnitudes. In contrast, for the SCM simulations, CRH decreases for $w_{\max} < 3$ cm/s. This seems to be a consequence of the local maximum in RH at the freezing level in these runs (Figure 9): As the freezing level shifts upward, these high values are weighted less strongly in the calculation of the column integrals (equation (6)). As previously noted, there is a dramatic increase in humidity with increasing LSF, particularly between the W0 and W1 simulations, which is largely consistent between the two models. However, in contrast to the CRM, the highest CRH values in the SCM do not occur for the strongest forcing, due to the nonmonotonic changes in RH in the lower troposphere (Figure 9). CWV increases strongly with SST and, similar to CRH, is also markedly higher in the presence of even weak LSF. As seen in Figure 2, the trends with forcing magnitude are nonmonotonic, except in the T305 CRM runs.

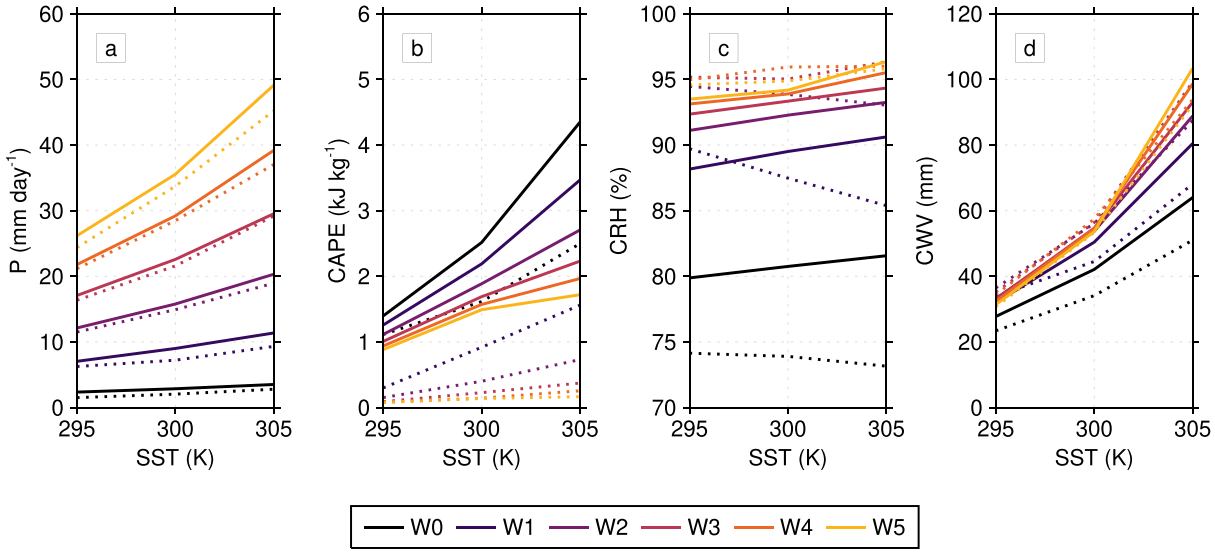

Figure 12. Line graphs showing the relationship between SST and (a) precipitation rate *P*, (b) CAPE, (c) column relative humidity (CRH), and (d) column water vapor (CWV) for the CRM (solid lines) and SCM (dotted lines) simulations. CAPE is computed from the (domain-averaged) temperature and moisture profiles using a pseudoadiabatic ascent from the lowest model level. CRH is computed as the ratio of column water vapor to saturation column water vapor, where the latter is taken with respect to water and ice at heights below and above the freezing level, respectively. All quantities are averaged over the final 25 days of each simulation.

4.5. Precipitation Relationships

As noted in section 1, one major advantage of our simulation methodology is that it allows us to represent a much wider variety of atmospheric states than is typically achieved in RCE or WTG simulations. This in turn permits the exploration of various physical relationships in the model across a broad parameter space. As an illustration, Figure 13 plots domain-averaged precipitation rate against the other three variables considered in the previous section: CAPE, CRH, and CWV.

We see a general decrease in precipitation with CAPE, although quantitatively, the relationship varies both with SST and between models. This tendency reflects the increase in *P* and RH with LSF (via equation (5)) and the decrease in CAPE with saturation fraction (via equation (8)): Stronger forcing promotes both heavier precipitation and, through convective detrainment, a more saturated column, giving lower CAPE under the

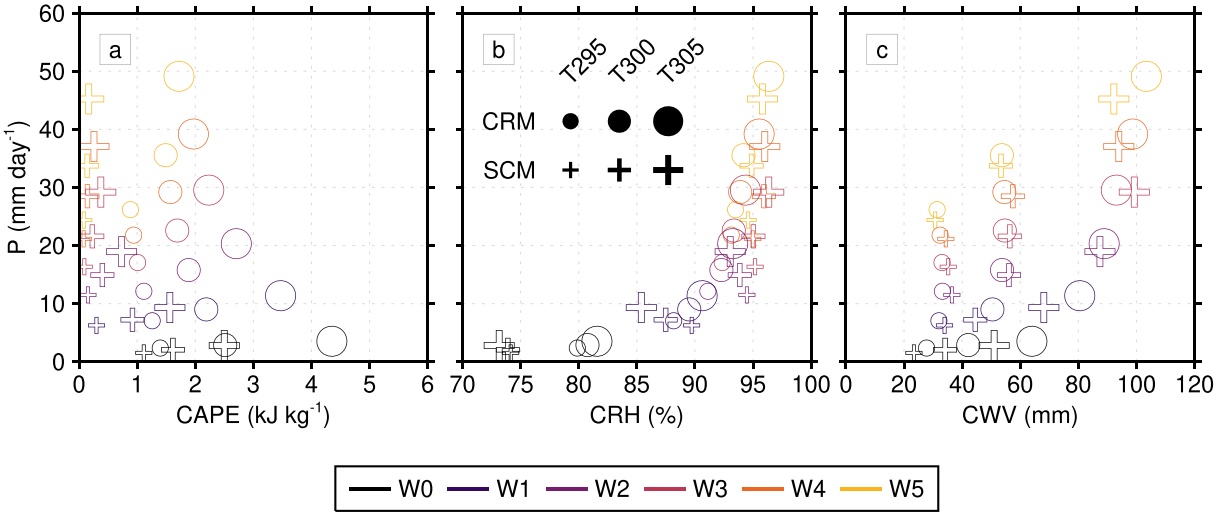

Figure 13. Scatter plots showing precipitation rate (*P*) as a function of (a) CAPE, (b) column relative humidity (CRH), and (c) column water vapor (CWV). Circles and crosses show results from CRM and SCM simulations, respectively, with symbol color indicating the LSF and symbol size indicating the SST. All quantities are averaged over the final 25 days of each simulation.

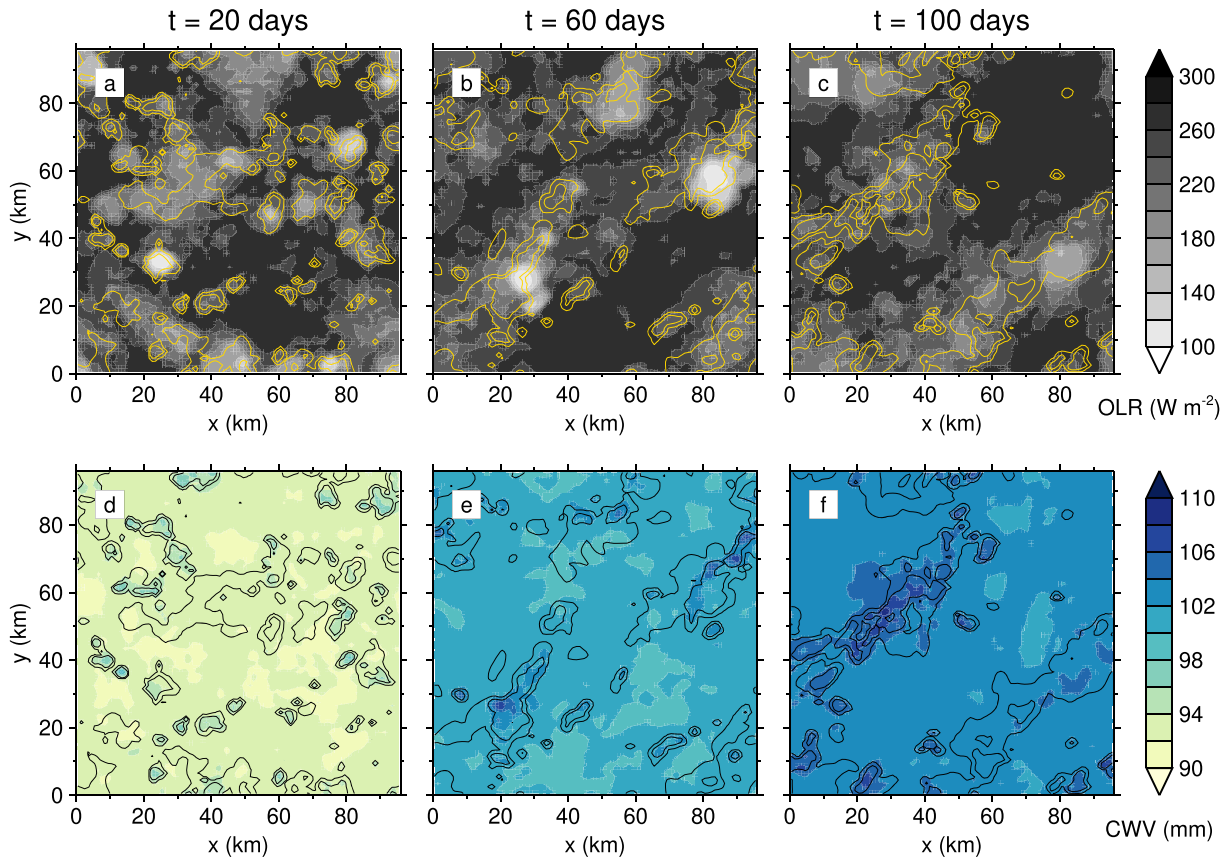

Figure 14. Maps of instantaneous (top) outgoing longwave radiation (OLR) and (bottom) column water vapor (CWV) from the T305–W5 CRM simulation at (left to right) t = 20, 60, and 100 days. Contours show the surface rain rate (1 and 10 mm/hr).

zero-buoyancy plume approximation. This finding is broadly consistent with observations, which show that large convective area fractions and area-averaged precipitation are associated with low-to-moderate CAPE (Davies et al., 2013; Louf et al., 2019).

For both CRH and CWV the relationship with P is strongly nonlinear, with a clear pickup in precipitation at some critical value. The critical value is approximately fixed for CRH but varies with temperature for CWV. Similar relationships are seen in numerous observations of the tropical atmosphere (Bretherton et al., 2004; Holloway & Neelin, 2009; Kuo et al., 2018; Rushley et al., 2018; Schiro et al., 2016). On short (convective) time scales, this behavior is argued to be a result of the sensitivity of the shallow-to-deep convective transition to lower-free-tropospheric humidity via entrainment (Holloway & Neelin, 2009; Kuo et al., 2017; Sahany et al., 2012). However, in our simulations, the precipitation rate is strongly constrained by the imposed forcing. Therefore, as argued by Singh et al. (2019), the CRH-P (and CWV-P) relationship results not from the sensitivity of convection to environmental humidity but from the increase in convective detrainment with increasing precipitation rate.

4.6. Convective Organization

As noted in section 4.1, the high-SST (T305), strongly forced (W3–5) CRM simulations are characterized by the development of organized convective structures, with coherent mesoscale outflows that drive fluctuations in domain-average CWV. The organization in these runs is markedly different from the convective aggregation seen in simulations of RCE. The latter typically show one or more well-defined clusters or lines of active convection surrounded by much drier regions, characterized by low values of CWV and large OLR (e.g., Wing & Emanuel, 2014, their Figures 1 and 3). In contrast, in our simulations, cloudy and precipitating regions are less spatially confined, and there is limited variability in CWV across the domain (Figure 14). As a result, diagnostics that are typically used to study convective aggregation, such as the spatial variance of MSE (Wing & Emanuel, 2014), are of limited use here.

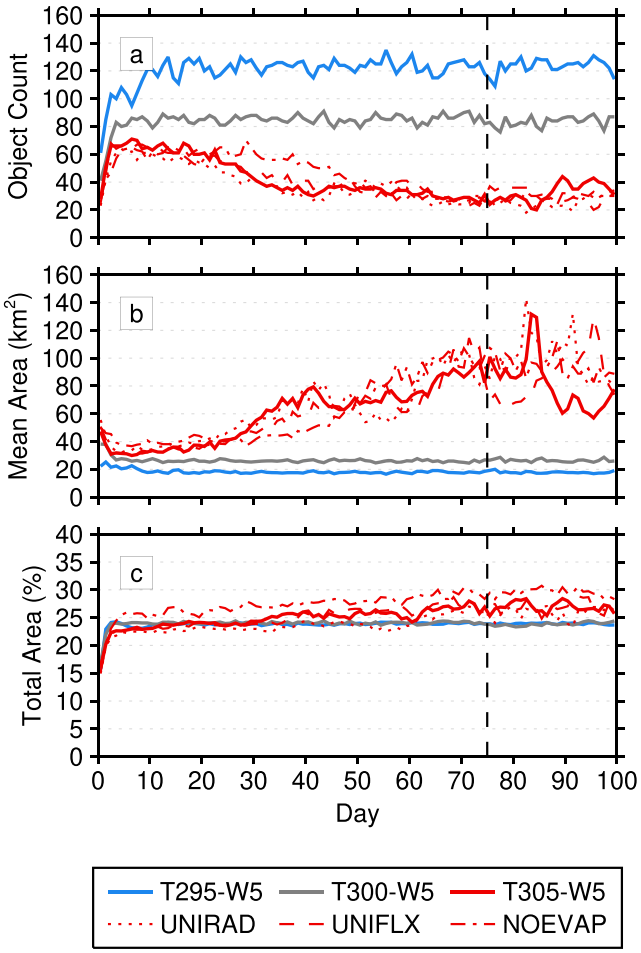

Figure 15. Time series of daily averaged (a) object count, (b) mean object area, and (c) total object area, expressed as a percentage of the domain area (9,216 km^2), for the W5 simulations at each SST and the three sensitivity runs.

To characterize organization, we identify contiguous precipitation objects at every output time, using a threshold of 1 mm/hr, and store the number of objects and the mean and total object area. These statistics, averaged to daily resolution, are shown in Figure 15 for the W5 simulations at each of the three SSTs. For the T295 and T300 cases, object properties stabilize within the first 10 days. In contrast, in the the T305 run, organization leads to a decrease in object count and an increase in mean object area between approximately Days 20 and 70, with large fluctuations in the latter quantity thereafter. Comparing the T295 and T300 runs, we see an increase in mean object area and a decrease in object count with SST. These changes cancel out, so that the total object area remains constant (at around 25% of the domain). However, organization leads to a slightly higher total object area in the T305 simulation.

As a first step toward understanding the processes leading to convective organization in RCDE, a set of three sensitivity runs were performed for the T305–W5 case. In the first run, UNIRAD, local radiation feedbacks were eliminated by applying horizontally averaged radiative heating profiles at every grid point. In the second run, UNIFLX, radiation feedbacks were permitted, but local surface flux feedbacks were removed by applying the same horizontal averaging to the surface fluxes of θ and r. In the third run, NOEVAP, convective cold pools were suppressed by switching off evaporation of rain and evaporation of melting snow and graupel in the Morrison microphysics scheme. Snapshots at $t = 100$ days from each of these runs are shown in Figure 16. These can be compared with the corresponding plots for the standard T305–W5 run in Figures 14c and 14f. Precipitation object statistics for these runs are also shown in Figure 15.

In simulations of RCE, radiation feedbacks have been shown to be essential for nonrotating convective self-aggregation to occur, while surface flux feedbacks are favorable but not always necessary for aggregation (Bretherton et al., 2005; Holloway & Woolnough, 2016; Muller & Held, 2012; Wing & Emanuel, 2014;

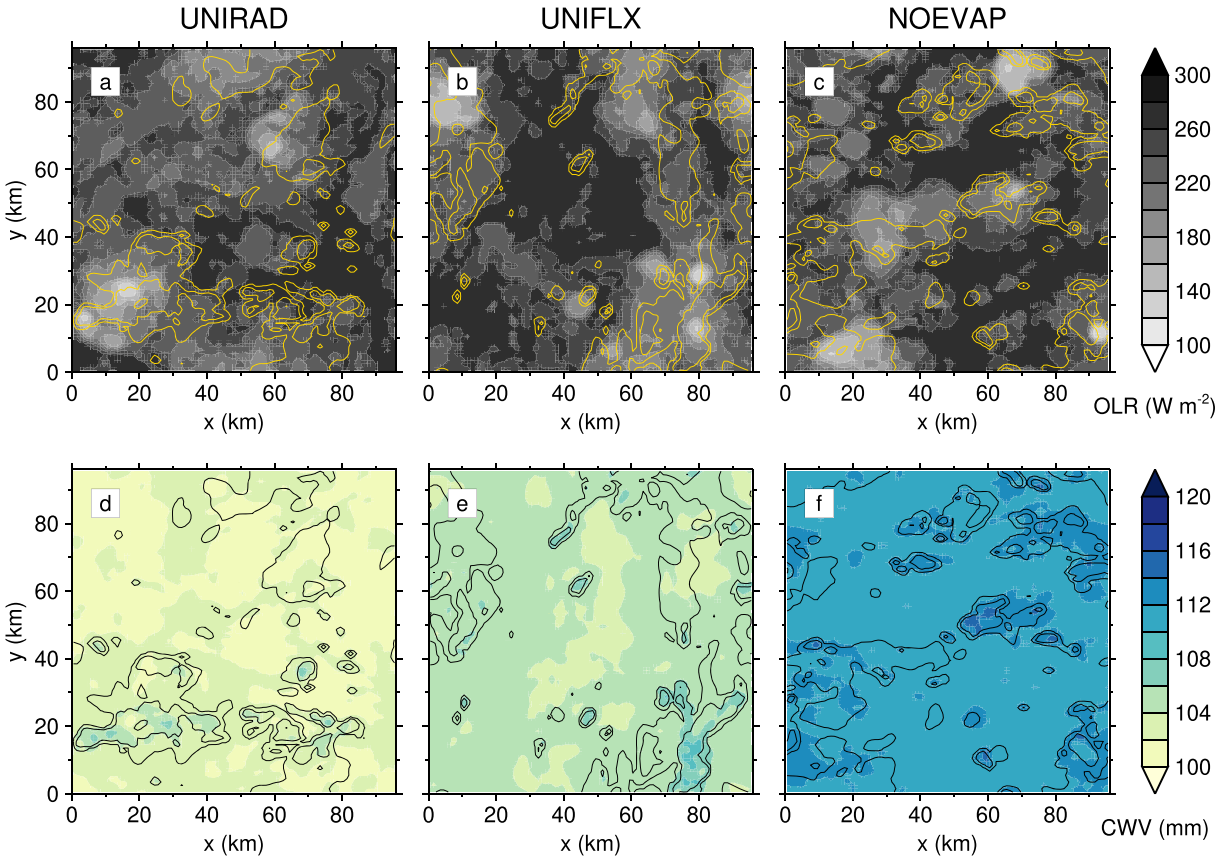

Figure 16. As in Figure 14 but for the (left to right) UNIRAD, UNIFLX, and NOEVAP simulations at $t = 100$ days. Note that the scale for CWV differs from that in Figure 14.

Wing & Cronin, 2016). On the other hand, the presence of cold pools has been found to delay aggregation or suppress it entirely for small domains (Jeevanjee & Romps, 2013). In contrast, Figures 15 and 16 suggest that the organization in our RCDE simulations is largely insensitive to these processes. All three sensitivity runs show the same basic evolution in terms of precipitation object characteristics, and the equilibrium state remains broadly consistent and quite distinct from that in aggregated RCE.

Further investigation is clearly required to elucidate the mechanisms leading to organization of convection in simulations of RCDE.

5. Conclusions

This study sought to highlight a potential addition to the existing arsenal of small-domain CRM and SCM simulation frameworks, namely, RCDE. In this framework, convection is simulated in the presence of a horizontally homogeneous fixed SST and a time-invariant large-scale vertical velocity velocity profile w_{LS}. The resulting equilibrium state is characterized by a three-way balance between adiabatic and radiative cooling and convective heating, with the relative contribution of radiation decreasing with increasing w_{LS}. An appealing characteristic of RCDE is the ability to simulate a much broader range of equilibrium states than is typically seen in simulations of RCE or those applying the WTG approximation or other related representations of the large-scale circulation.

To investigate the basic characteristics of the RCDE state and its dependence on model type, a suite of 18 simulations, employing three SSTs and six LSF magnitudes (including the RCE case with $w_{LS} = 0$), were performed using one CRM and one SCM. We find that the RCDE state is both warmer and moister than the corresponding RCE state, particularly at high SSTs. Stronger forcing promotes larger domain-averaged precipitation accompanied by higher static stability and larger CWV and CRH. Taken together, the suite

of simulations reproduces (at least qualitatively) the observed positive and strongly nonlinear relationships between CRH/CWV and precipitation and highlights a temperature-dependent inverse relationship between CAPE and precipitation. In a companion study, Singh et al. (2019) develop a simple bulk-plume model that reproduces these features, offering insight into the observed relationship between humidity, instability, and precipitation in the tropics on intraseasonal and longer time scales.

An interesting feature of the CRM simulations is that, for the combination of a high SST and strong forcing, convection becomes spontaneously organized into clusters, separated by broader precipitation-free regions. Unlike the self-aggregated convective states achieved in some RCE simulations, the resulting equilibria are not characterized by strong gradients in CWV or OLR. Furthermore, sensitivity tests suggest that convective cold pools and local radiation and surface flux feedbacks are not necessary for this organization to occur. The equilibrium state in these runs is characterized by extremely higher CWV values (>90 mm); thus, the processes leading to organization may not be relevant to present-day climates. Nevertheless, it would be interesting to perform further sensitivity experiments, considering factors such as domain size, grid spacing, and the choice of subgrid parameterizations. One could also explore the impact of including horizontal moisture advection as part of the imposed forcing, similar to what has been done for WTG simulations (Sessions et al., 2015).

The rich response of the two models tested here to the imposed dynamical forcing suggests that RCDE is a useful rung in the model hierarchy with which to study convection and its interaction with the large-scale atmosphere. For example, the apparent overstabilization of the SCM relative to the CRM may provide insight into deficiencies in the way cloud-base mass flux is determined within the SCM convection parameterization. Comparison across a broader range of CRMs and SCMs is clearly needed. We believe that the suite of simulations performed for this study (or a subset thereof) would constitute a natural extension to RCEMIP, once the results of that study have been digested. An intercomparison of multiple CRMs and SCMs would shed light on the robustness of the RCDE state and provide insight into the behavior of different convection parameterization schemes under a wide range of environmental conditions.

Acknowledgments
R. A. Warren was funded by the National Environmental Science Program through the Earth Systems and Climate Change Hub. M. S. Singh was supported by an Australian Research Council (ARC) Discovery Early Career Researcher Award (DE190100866). The authors also acknowledge support from the ARC Centre of Excellence for Climate Extremes (CE170100023). Computational resources and services from the National Computational Infrastructure, which is supported by the Australian Government, are gratefully acknowledged. We thank Alison Wing for providing additional details on the simulation configurations for RCEMIP and Mike Whitall for useful discussions regarding the UM convection scheme. We also thank two anonymous reviewers, Associate Editor Juliana Dias, and Editor-in-Chief Robert Pincus for their constructive comments on an earlier draft of this manuscript. UM simulation output and CM1 code and input files are available through the institutional repository Bridges (at https://doi.org/10.26180/5ccfd3e10829a).

References

Abdel-Lathif, A. Y., Roehrig, R., Beau, I., & Douville, H. (2018). Single-column modeling of convection during the CINDY2011/DYNAMO field campaign with the CNRM climate model version 6. *Journal of Advances in Modeling Earth Systems*, *10*, 578–602. https://doi.org/10.1002/2017MS001077

Anber, U., Wang, S., & Sobel, A. (2014). Response of atmospheric convection to vertical wind shear: Cloud-system-resolving simulations with parameterized large-scale circulation. Part I: Specified radiative cooling. *Journal of the Atmospheric Sciences*, *71*(8), 2976–2993.

Bechtold, P., Redelsperger, J.-L., Beau, I., Blackburn, M., Brinkop, S., Grandper, J.-Y., et al. (2000). A GCSS model intercomparison for a tropical squall line observed during TOGA-COARE. II: Intercomparison of single-column models and a cloud-resolving model. *Quarterly Journal of the Royal Meteorological Society*, *126*(564), 865–888.

Blossey, P. N., Bretherton, C. S., & Wyant, M. C. (2009). Subtropical low cloud response to a warmer climate in a superparameterized climate model. Part II: Column modeling with a cloud resolving model. *Journal of Advances in Modeling Earth Systems*, *1*, 8. https://doi.org/10.3894/JAMES.2009.1.8

Borges, R., Carmona, M., Costa, B., & Don, W. S. (2008). An improved weighted essentially non-oscillatory scheme for hyperbolic conservation laws. *Journal of Computational Physics*, *227*(6), 3191–3211.

Bretherton, C. S., Blossey, P. N., & Khairoutdinov, M. (2005). An energy-balance analysis of deep convective self-aggregation above uniform SST. *Journal of the Atmospheric Sciences*, *62*(12), 4273–4292.

Bretherton, C. S., Peters, M. E., & Back, L. E. (2004). Relationships between water vapor path and precipitation over the tropical oceans. *Journal of Climate*, *17*(7), 1517–1528.

Brown, A., Beare, R., Edwards, J., Lock, A., Keogh, S., Milton, S., & Walters, D. (2008). Upgrades to the boundary-layer scheme in the Met Office numerical weather prediction model. *Boundary-Layer Meteorology*, *128*(1), 117–132.

Bryan, G. H. (2017). The governing equations for CM1. http://www2.mmm.ucar.edu/people/bryan/cm1/cm1&urluscore;equations.pdf

Bryan, G. H., & Fritsch, J. M. (2002). A benchmark simulation for moist nonhydrostatic numerical models. *Monthly Weather Review*, *130*(12), 2917–2928.

Coffer, B. E., & Parker, M. D. (2017). Simulated supercells in nontornadic and tornadic VORTEX2 environments. *Monthly Weather Review*, *145*(1), 149–180.

Cronin, T. W., & Wing, A. A. (2017). Clouds, circulation, and climate sensitivity in radiative-convective equilibrium channel model. *Journal of Advances in Modeling Earth Systems*, *9*, 2883–2905. https://doi.org/10.1002/2017MS001111

Daleu, C. L., Plant, R. S., Woolnough, S. J., Sessions, S., Herman, M. J., Sobel, A., et al. (2015). Intercomparison of methods of coupling between convection and large-scale circulation: 1. Comparison over uniform surface conditions. *Journal of Advances in Modeling Earth Systems*, *7*, 1576–1601. https://doi.org/10.1002/2015MS000468

Daleu, C. L., Plant, R. S., Woolnough, S. J., Sessions, S., Herman, M. J., Sobel, A., et al. (2016). Intercomparison of methods of coupling between convection and large-scale circulation: 2. Comparison over nonuniform surface conditions. *Journal of Advances in Modeling Earth Systems*, *8*, 387–405. https://doi.org/10.1002/2015MS000570

Davies, L., Jakob, C., Cheung, K., Del Genio, A., Hill, A., Hume, T., et al. (2013). A single-column model ensemble approach applied to the TWP-ICE experiment. *Journal of Geophysical Research: Atmospheres*, *118*, 6544–6563. https://doi.org/10.1002/jgrd.50450

Davies, L., Jakob, C., May, P., Kumar, V., & Xie, S. (2013). Relationships between the large-scale atmosphere and the small-scale convective state for Darwin, Australia. *Journal of Geophysical Research: Atmospheres*, *118*, 11–534. https://doi.org/10.1002/jgrd.50645

Deardorff, J. W. (1980). Stratocumulus-capped mixed layers derived from a three-dimensional model. *Boundary Layer Meteorology*, *18*(4), 495–527.

Dunion, J. P. (2011). Rewriting the climatology of the tropical North Atlantic and Caribbean Sea atmosphere. *Journal of Climate*, *24*(3), 893–908.

Edman, J. P., & Romps, D. M. (2014). An improved weak pressure gradient scheme for single-column modeling. *Journal of the Atmospheric Sciences*, *71*(7), 2415–2429.

Edman, J. P., & Romps, D. M. (2015). Self-consistency tests of large-scale dynamics parameterizations for single-column modeling. *Journal of Advances in Modeling Earth Systems*, *7*, 320–334. https://doi.org/10.1002/2014MS000378

Edwards, J., & Slingo, A. (1996). Studies with a flexible new radiation code. I: Choosing a configuration for a large-scale model. *Quarterly Journal of the Royal Meteorological Society*, *122*(531), 689–719.

Fridlind, A., Ackerman, A., Chaboureau, J.-P., Fan, J., Grabowski, W. W., Hill, A., et al. (2012). A comparison of TWP-ICE observational data with cloud-resolving model results. *Journal of Geophysical Research: Atmospheres*, *117*, D05204. https://doi.org/10.1029/2011JD016595

Fritsch, J., & Chappell, C. (1980). Numerical prediction of convectively driven mesoscale pressure systems. Part I: Convective parameterization. *Journal of the Atmospheric Sciences*, *37*(8), 1722–1733.

Gregory, D., & Rowntree, P. (1990). A mass flux convection scheme with representation of cloud ensemble characteristics and stability-dependent closure. *Monthly Weather Review*, *118*(7), 1483–1506.

Herman, M. J., & Raymond, D. J. (2014). WTG cloud modeling with spectral decomposition of heating. *Journal of Advances in Modeling Earth Systems*, *6*, 1121–1140. https://doi.org/10.1002/2014MS000359

Holloway, C. E., & Neelin, J. D. (2009). Moisture vertical structure, column water vapor, and tropical deep convection. *Journal of the Atmospheric Sciences*, *66*(6), 1665–1683.

Holloway, C. E., Wing, A. A., Bony, S., Muller, C., Masunaga, H., LâĂŹEcuyer, T. S., et al. (2017). Observing convective aggregation. *Surveys in Geophysics*, *38*(6), 1199–1236.

Holloway, C. E., & Woolnough, S. J. (2016). The sensitivity of convective aggregation to diabatic processes in idealized radiative-convective equilibrium simulations. *Journal of Advances in Modeling Earth Systems*, *8*, 166–195. https://doi.org/10.1002/2015MS000511

Jakob, C., Singh, M., & Jungandreas, L. (2019). Radiative convective equilibrium and organized convection: An observational perspective. *Journal of Geophysical Research: Atmospheres*, *124*, 5418–5430. https://doi.org/10.1029/2018JD030092

Jeevanjee, N., & Romps, D. M. (2013). Convective self-aggregation, cold pools, and domain size. *Geophysical Research Letters*, *40*, 994–998. https://doi.org/10.1002/grl.50204

Jiang, G.-S., & Shu, C.-W. (1996). Efficient implementation of weighted ENO schemes. *Journal of Computational Physics*, *126*(1), 202–228.

Jiménez, P. A., Dudhia, J., González-Rouco, J. F., Navarro, J., Montávez, J. P., & García-Bustamante, E. (2012). A revised scheme for the WRF surface layer formulation. *Monthly Weather Review*, *140*(3), 898–918.

Johnson, D., Tao, W., Simpson, J., & Sui, C. (2002). A study of the response of deep tropical clouds to large-scale thermodynamic forcings. Part I: Modeling strategies and simulations of TOGA COARE convective systems. *Journal of the Atmospheric Sciences*, *59*(24), 3492–3518.

Klemp, J. B., & Wilhelmson, R. B. (1978). The simulation of three-dimensional convective storm dynamics. *Journal of the Atmospheric Sciences*, *35*(6), 1070–1096.

Kuang, Z. (2008). Modeling the interaction between cumulus convection and linear gravity waves using a limited-domain cloud system–resolving model. *Journal of the Atmospheric Sciences*, *65*(2), 576–591.

Kuo, Y.-H., Neelin, J. D., & Mechoso, C. R. (2017). Tropical convective transition statistics and causality in the water vapor–precipitation relation. *Journal of the Atmospheric Sciences*, *74*(3), 915–931.

Kuo, Y.-H., Schiro, K. A., & Neelin, J. D. (2018). Convective transition statistics over tropical oceans for climate model diagnostics: Observational baseline. *Journal of the Atmospheric Sciences*, *75*(5), 1553–1570.

Li, X., Janiga, M. A., Wang, S., Tao, W.-K., Rowe, A., Xu, W., et al. (2018). Evolution of precipitation structure during the november DYNAMO MJO event: Cloud-resolving model intercomparison and cross validation using radar observations. *Journal of Geophysical Research: Atmospheres*, *123*, 3530–3555. https://doi.org/10.1002/2017JD027775

Lock, A. (2001). The numerical representation of entrainment in parameterizations of boundary layer turbulent mixing. *Monthly Weather Review*, *129*(5), 1148–1163.

Lock, A., Brown, A., Bush, M., Martin, G., & Smith, R. (2000). A new boundary layer mixing scheme. Part I: Scheme description and single-column model tests. *Monthly Weather Review*, *128*(9), 3187–3199.

Louf, V., Jakob, C., Protat, A., Bergmann, M., & Narsey, S. (2019). The relationship of cloud number and size with their large-scale environment in deep tropical convection. *Geophysical Research Letters*, *46*, 9203–9212. https://doi.org/10.1029/2019GL083964

Manabe, S., & Strickler, R. F. (1964). Thermal equilibrium of the atmosphere with a convective adjustment. *Journal of the Atmospheric Sciences*, *21*(4), 361–385.

Manners, J., Edwards, J. M., Hill, P., & Thelen, J.-C. (2015). SOCRATES (Suite Of Community RAdiative Transfer codes based on Edwards and Slingo) Technical Guide. Met Office, https://code.metoffice.gov.uk/trac/socrates

Martin, G. M., Klingaman, N. P., & Moise, A. F. (2017). Connecting spatial and temporal scales of tropical precipitation in observations and the MetUM-GA6. *Geoscientific Model Development*, *10*(1), 105–126.

May, P. T., Mather, J. H., Vaughan, G., Jakob, C., McFarquhar, G. M., Bower, K. N., & Mace, G. G. (2008). The Tropical Warm Pool International Cloud Experiment. *Bulletin of the American Meteorological Society*, *89*(5), 629–646.

Möller, F. (1963). On the influence of changes in the CO2 concentration in air on the radiation balance of the Earth's surface and on the climate. *Journal of Geophysical Research*, *68*(13), 3877–3886.

Morcrette, C. J. (2012). Improvements to a prognostic cloud scheme through changes to its cloud erosion parametrization. *Atmospheric Science Letters*, *13*(2), 95–102.

Morrison, H., Curry, J., & Khvorostyanov, V. (2005). A new double-moment microphysics parameterization for application in cloud and climate models. Part I: Description. *Journal of the Atmospheric Sciences*, *62*(6), 1665–1677.

Muller, C. J., & Held, I. M. (2012). Detailed investigation of the self-aggregation of convection in cloud-resolving simulations. *Journal of the Atmospheric Sciences*, *69*(8), 2551–2565.

Muller, C. J., O'Gorman, P. A., & Back, L. E. (2011). Intensification of precipitation extremes with warming in a cloud-resolving model. *Journal of Climate*, *24*(11), 2784–2800.

O'Gorman, P. A., & Schneider, T. (2009). The physical basis for increases in precipitation extremes in simulations of 21st-century climate change. *Proceedings of the National Academy of Sciences*, *106*(35), 14773–14777.

Petch, J., Hill, A., Davies, L., Fridlind, A., Jakob, C., Lin, Y., et al. (2014). Evaluation of intercomparisons of four different types of model simulating TWP-ICE. *Quarterly Journal of the Royal Meteorological Society*, *140*(680), 826–837.
Randall, D. A., & Cripe, D. G. (1999). Alternative methods for specification of observed forcing in single-column models and cloud system models. *Journal of Geophysical Research: Atmospheres*, *104*(D20), 24,527–24,545. https://doi.org/10.1029/1999JD900765
Raymond, D. J., & Zeng, X. (2005). Modelling tropical atmospheric convection in the context of the weak temperature gradient approximation. *Quarterly Journal of the Royal Meteorological Society*, *131*(608), 1301–1320.
Redelsperger, J.-L., Brown, P., Guichard, F., How, C., Kawasima, M., Lang, S., et al. (2000). A GCSS model intercomparison for a tropical squall line observed during TOGA-COARE. I: Cloud-resolving models. *Quarterly Journal of the Royal Meteorological Society*, *126*(564), 823–863.
Romps, D. M. (2011). Response of tropical precipitation to global warming. *Journal of the Atmospheric Sciences*, *68*(1), 123–138.
Romps, D. M. (2012a). Numerical tests of the weak pressure gradient approximation. *Journal of the Atmospheric Sciences*, *69*(9), 2846–2856.
Romps, D. M. (2012b). Weak pressure gradient approximation and its analytical solutions. *Journal of the Atmospheric Sciences*, *69*(9), 2835–2845.
Romps, D. M. (2014). An analytical model for tropical relative humidity. *Journal of Climate*, *27*(19), 7432–7449.
Romps, D. M. (2016). Clausius–clapeyron scaling of CAPE from analytical solutions to RCE. *Journal of the Atmospheric Sciences*, *73*(9), 3719–3737.
Rushley, S., Kim, D., Bretherton, C., & Ahn, M.-S. (2018). Reexamining the nonlinear moisture-precipitation relationship over the tropical oceans. *Geophysical Research Letters*, *45*, 1133–1140. https://doi.org/10.1002/2017GL076296
Sahany, S., Neelin, J. D., Hales, K., & Neale, R. B. (2012). Temperature-moisture dependence of the deep convective transition as a constraint on entrainment in climate models. *Journal of the Atmospheric Sciences*, *69*(4), 1340–1358.
Schiro, K. A., Neelin, J. D., Adams, D. K., & Lintner, B. R. (2016). Deep convection and column water vapor over tropical land versus tropical ocean: A comparison between the Amazon and the tropical western Pacific. *Journal of the Atmospheric Sciences*, *73*(10), 4043–4063.
Seeley, J. T., & Romps, D. M. (2015). Why does tropical convective available potential energy (CAPE) increase with warming? *Geophysical Research Letters*, *42*, 10–429. https://doi.org/10.1002/2015GL066199
Sessions, S. L., Herman, M. J., & Sentić, S. (2015). Convective response to changes in the thermodynamic environment in idealized weak temperature gradient simulations. *Journal of Advances in Modeling Earth Systems*, *7*, 712–738. https://doi.org/10.1002/2015MS000446
Sessions, S. L., Sugaya, S., Raymond, D. J., & Sobel, A. H. (2010). Multiple equilibria in a cloud-resolving model using the weak temperature gradient approximation. *Journal of Geophysical Research: Atmospheres*, *115*, D12110. https://doi.org/10.1029/2009JD013376
Singh, M. S., & O'Gorman, P. A. (2013). Influence of entrainment on the thermal stratification in simulations of radiative-convective equilibrium. *Geophysical Research Letters*, *40*, 4398–4403. https://doi.org/10.1002/grl.50796
Singh, M. S., & O'Gorman, P. A. (2015). Increases in moist-convective updraught velocities with warming in radiative-convective equilibrium. *Quarterly Journal of the Royal Meteorological Society*, *141*(692), 2828–2838.
Singh, M. S., Warren, R. A., & Jakob, C. (2019). A steady-state model for the relationship between humidity, instability, and precipitation in the tropics. *Journal of Advances in Modeling Earth Systems*, *11*, 3973–3994. https://doi.org/10.1029/2019MS001686
Sobel, A. H., & Bellon, G. (2009). The effect of imposed drying on parameterized deep convection. *Journal of the Atmospheric Sciences*, *66*(7), 2085–2096.
Sobel, A. H., Bellon, G., & Bacmeister, J. (2007). Multiple equilibria in a single-column model of the tropical atmosphere. *Geophysical Research Letters*, *34*, L22804. https://doi.org/10.1029/2007GL031320
Sobel, A. H., & Bretherton, C. S. (2000). Modeling tropical precipitation in a single column. *Journal of Climate*, *13*(24), 4378–4392.
Van Weverberg, K., Boutle, I. A., Morcrette, C. J., & Newsom, R. K. (2016). Towards retrieving critical relative humidity from ground-based remote-sensing observations. *Quarterly Journal of the Royal Meteorological Society*, *142*(700), 2867–2881.
Walters, D., Baran, A., Boutle, I., Brooks, M., Earnshaw, P., Edwards, J., et al. (2019). The Met Office Unified Model Global Atmosphere 7.0/7.1 and JULES Global Land 7.0 configurations. *Geoscientific Model Development*, *12*, 1909–1963.
Wang, S., & Sobel, A. H. (2011). Response of convection to relative sea surface temperature: Cloud-resolving simulations in two and three dimensions. *Journal of Geophysical Research*, *116*, D11119. https://doi.org/10.1029/2010JD015347
Wang, S., & Sobel, A. (2012). Impact of imposed drying on deep convection in a cloud-resolving model. *Journal of Geophysical Research: Atmospheres*, *117*, D02112. https://doi.org/10.1029/2011JD016847
Wang, S., Sobel, A. H., Fridlind, A., Feng, Z., Comstock, J. M., Minnis, P., & Nordeen, M. L. (2015). Simulations of cloud-radiation interaction using large-scale forcing derived from the CINDY/DYNAMO northern sounding array. *Journal of Advances in Modeling Earth Systems*, *7*, 1472–1498. https://doi.org/10.1002/2015MS000461
Wang, S., Sobel, A. H., & Kuang, Z. (2013). Cloud-resolving simulation of TOGA-COARE using parameterized large-scale dynamics. *Journal of Geophysical Research: Atmospheres*, *118*, 6290–6301. https://doi.org/10.1002/jgrd.50510
Wang, S., Sobel, A. H., & Nie, J. (2016). Modeling the MJO in a cloud-resolving model with parameterized large-scale dynamics: Vertical structure, radiation, and horizontal advection of dry air. *Journal of Advances in Modeling Earth Systems*, *8*, 121–139. https://doi.org/10.1002/2015MS000529
Webster, P. J., & Lukas, R. (1992). TOGA COARE: The coupled ocean-atmosphere response experiment. *Bulletin of the American Meteorological Society*, *73*(9), 1377–1416.
Wilson, D. R., & Ballard, S. P. (1999). A microphysically based precipitation scheme for the UK Meteorological Office Unified Model. *Quarterly Journal of the Royal Meteorological Society*, *125*(557), 1607–1636.
Wilson, D. R., Bushell, A. C., Kerr-Munslow, A. M., Price, J. D., & Morcrette, C. J. (2008a). PC2: A prognostic cloud fraction and condensation scheme. I: Scheme description. *Quarterly Journal of the Royal Meteorological Society*, *134*(637), 2093–2107.
Wilson, D. R., Bushell, A., Kerr-Munslow, A. M., Price, J. D., Morcrette, C. J., & Bodas-Salcedo, A. (2008b). PC2: A prognostic cloud fraction and condensation scheme. II: Climate model simulations. *Quarterly Journal of the Royal Meteorological Society*, *134*(637), 2109–2125.
Wing, A. A., & Cronin, T. W. (2016). Self-aggregation of convection in long channel geometry. *Quarterly Journal of the Royal Meteorological Society*, *142*(694), 1–15.
Wing, A. A., & Emanuel, K. A. (2014). Physical mechanisms controlling self-aggregation of convection in idealized numerical modeling simulations. *Journal of Advances in Modeling Earth Systems*, *6*, 59–74. https://doi.org/10.1002/2013MS000269
Wing, A. A., Emanuel, K., Holloway, C. E., & Muller, C. (2017). Convective self-aggregation in numerical simulations: A review. *Surveys in Geophysics*, *38*(6), 1173–1197.
Wing, A. A., Reed, K. A., Satoh, M., Stevens, B., Bony, S., & Ohno, T. (2018). Radiative-convective equilibrium model intercomparison project. *Geoscientific Model Development*, *11*, 793–813.
Yoneyama, K., Zhang, C., & Long, C. N. (2013). Tracking pulses of the Madden-Julian oscillation. *Bulletin of the American Meteorological Society*, *94*(12), 1871–1891.